Ore Geology Reviews 117 (2020) 103264

Contents lists available at ScienceDirect

Ore Geology Reviews

journal homepage: www.elsevier.com/locate/oregeorev

三江特提斯带雀莫错碳酸盐岩铅锌矿床的成因:来自Sm-Nd等时年龄和Sr-S-Pb同位素组成的制约

第一标注

The origin of the Quemocuo carbonate-hosted Pb-Zn deposit in the Sanjiang Tethyan Belt, SW China: Constrained by Sm-Nd isochronic age and Sr-S-Pb isotope compositions

Huishan Zhang[a,b], Wenhua Ji[b], Xiaoyong Yang[a,*], Jia-Xi Zhou[c,*], Chao Sun[a], Zongyong Jia[d], Jun Hong[b], Pengrui Lv[b], Zhuang Zhao[a], Qi Hou[a]

[a] CAS Key Laboratory of Crust-Mantle Materials and Environments, School of Earth and Space Sciences, University of Science and Technology of China, Hefei 230026, China
[b] MNR Key Laboratory for the Study of Focused Magmatism and Giant Ore Deposits, Xi'an Center of Geological Survey, CGS, Xi'an 710054, China
[c] School of Resource Environment and Earth Sciences, Yunnan University, Kunming 650500, China
[d] NO.5 Institute of Geology and Mineral Resources Exploration, Xining 810028, China

ARTICLE INFO

Keywords:
Sm-Nd isochronic age
In situ S-Pb isotopes
Bulk Sr isotopes
Ore genesis
Quemocuo Pb-Zn deposit
Sanjiang Pb-Zn metallogenic belt

ABSTRACT

The newly discovered Quemocuo Pb-Zn deposit (7.1 Mt of sulfide ores, grading 1.65–7.17 wt% Pb and 1.13–5.7 wt% Zn) is located in the Tuotuohe area of the Sanjiang Tethyan metallogenic belt, SW China. The stratiform and veined ore body is hosted in the limestone of the Upper Permian Labuchari Formation and occur along the NE-trending fault. Four main mineralization stages are distinguished as follows: (i) pyrite + calcite + quartz, (ii) sphalerite + galena + pyrite + calcite + barite + quartz, (iii) galena + sphalerite + pyrite + calcite + barite + quartz, and (iv) calcite + dolomite. Sm-Nd dating of five calcite samples in stage II yielded an isochronic age of 34.3 ± 2.2 Ma (MSWD = 7.1), possibly reflecting the formation age of the Quemocuo Pb-Zn deposit. In situ sulfur isotopic compositions of the sulfides in stages I, II and III range from −29.5‰ to −26.5‰, −4.7‰ to +6.0‰, and +1.7‰ to +6.9‰, respectively. Such sulfur isotope signatures indicate bacterial sulfate reduction (BSR) and thermochemical sulfate reduction (TSR) of seawater or sulfate minerals. In situ Pb isotopic ratios indicate a similar origin for the sulfides in stages I, II and III, which all are related to metamorphic basement rocks and ore-hosting sedimentary strata. Initial $^{87}Sr/^{86}Sr$ ratios of sphalerite are 0.7085–0.7117, indicating a mixed source as suggested by in situ Pb isotopes. The Quemocuo Pb-Zn deposit was proposed to be a strata-bound and normal fault-controlled epigenetic deposit, with a mixed source of basement and strata, and even volcanic rocks. Our study suggests that the formation of the Quemocuo Pb-Zn deposit is related to the Cenozoic collision event between the Indian and Eurasian plates.

1. Introduction

Carbonate-hosted Pb-Zn deposits, as an important part of the sediment-hosted Pb-Zn deposits, are widely spread around the world (Leach et al., 2005, 2010). For example, they are widely distributed in Silesia area of Europe (Heijlen et al., 2003; Muchez et al., 2005), mid-continent region of the United States of America (Sverjensky, 1981), Pine Point of Canada (Powell and Macqueen, 1984) and Sanjiang belt of China (Zhang, 2010; Tian et al., 2011; Liu, 2012, Liu et al., 2015a, b, c, d; Liu et al., 2011, 2015e, 2016, 2017; Song et al., 2013, 2015, 2017; Zhang, 2014; Qian, 2014; Dong et al., 2015; Hou and Zhang, 2015; Zhang et al., 2017). The Sanjiang Pb-Zn metallogenic belt is an important part of the east Tethyan metallogenic belt, including the Tianshuihai, Tuotuohe, Yushu, Changdu and Lanping ore districts from northwest to southeast (Fig. 1). There are several famous sediment-hosted Pb-Zn deposits in the Sanjiang belt, such as the world-class Jinding Pb-Zn deposit (15 Mt Pb + Zn metal reserves; Xue et al., 2007; Tang et al., 2014), Huoshaoyun Pb-Zn deposit (16 Mt Pb + Zn metal reserves; Dong et al., 2015; Li et al., 2019), and Duocaima Pb-Zn deposit (6 Mt Pb + Zn metal reserves; Song et al., 2013, 2015; Guo, 2018).

The Tuotuohe ore district is located in the northwestern Sanjiang Pb-Zn metallogenic belt that contains over 20 Pb-Zn deposits with total Pb + Zn metal reserves over 10 Mt (Zhang, 2014), such as world-class Duocaima (Song et al., 2013, 2015; Guo, 2018), Chuduoqu (Zou et al., 2014; Chen et al., 2014a), Basihu (Dong, 2018), Nabaozhalong (Zhang

* Corresponding authors at: School of Resource Environment and Earth Sciences, Yunnan University, Kunming 650500, China.
E-mail addresses: xyyang@ustc.edu.cn (X. Yang), zhoujiaxi@ynu.edu.cn (J.-X. Zhou).

https://doi.org/10.1016/j.oregeorev.2019.103264
Received 15 June 2019; Received in revised form 5 October 2019; Accepted 29 November 2019
Available online 05 December 2019

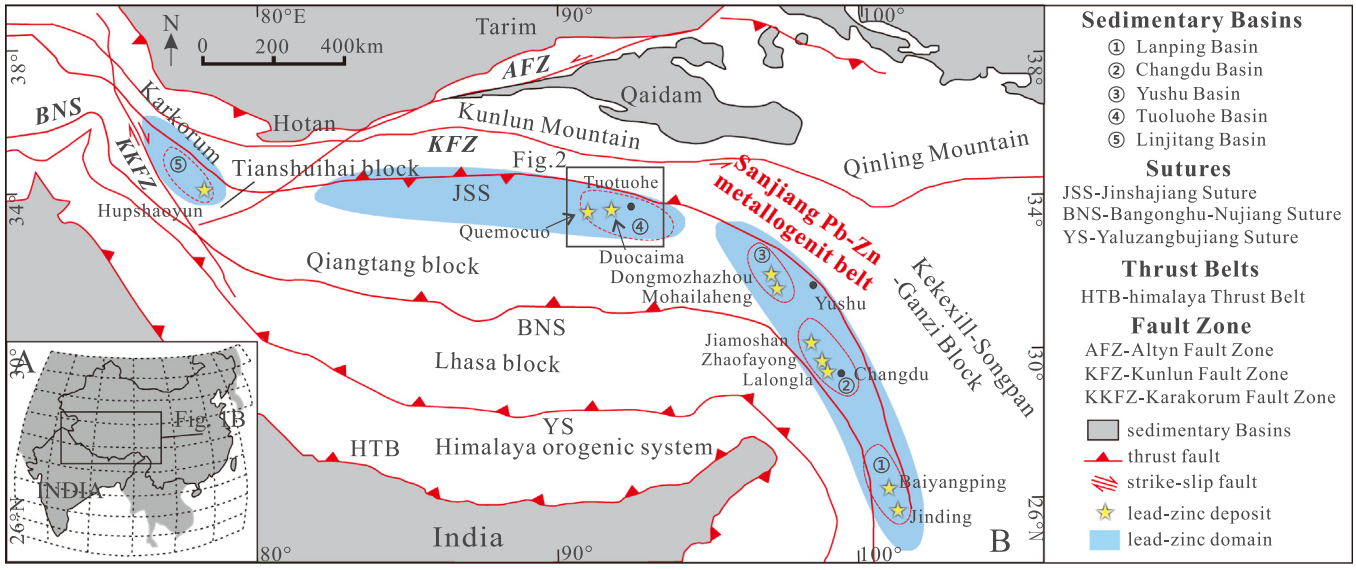

Fig. 1. A. The Location of the study area in Asia (simplified from Liu et al., 2014); B. Simplified tectonic map, showing the location of the Quemocuo deposit and the Sanjiang Pb-Zn metallogenic belt within the Tibetan plateau. Modified after Spurlin et al. (2005); Zhang (2010); Dong et al. (2015); Liu et al. (2016) and Li et al. (2019).

et al., 2008), and Queomocuo Pb-Zn deposits (Jia, 2014; Liu et al., 2015d). Also, these Pb-Zn deposits are mainly hosted in Permian to Paleogene carbonate and clastic rocks (Zhang, 2014). Recently, extensive studies were carried out on these deposits, especially for the world-class Duocaima Pb-Zn deposit (Zhang,2010; Wang et al., 2012; Song et al., 2009,2013, 2015; Zhang, 2014; Hao, 2014, Hao et al., 2015; Qian., 2014; Liu et al., 2015a,b,c; Yang, 2017; Guo, 2018; Jia et al., 2018; Yao et al., 2019). However, the ore genesis of these deposits is still unclear, some researchers argued that these deposits belong to the Mississippi Valley-type (MVT) (Song et al., 2009, 2013, 2015; Zhang, 2014; Hao, 2014; Hao et al., 2015; Liu et al., 2015a,b,c), whereas other studies presented the viewpoint of epithermal type that is related to the magmatism (Qian., 2014; Yang, 2017; Guo, 2018; Jia et al., 2018). The above controversy is mainly due to the lack of effective geochronology and isotope geochemical constraints.

The isotope geochemistry (such as S, Pb, and Sr system) have been widely used to determine the source and evolution of hydrothermal fluids (Carr et al., 1995; Zhou et al., 2001; Wilkinson et al., 2005; Li et al., 2015; Zhou et al., 2016a,b, 2018a,b,c). Besides, microbeam analytical techniques provide an ideal way to obtain crucial microscale chemical and isotopic information, which is essential for understanding the genesis of hydrothermal ore deposits and is benefit for revealing the metallogenic process and depositional environment of hydrothermal systems (Barker et al., 2009; Deng et al., 2017; Jin et al., 2016; Luo et al., 2019; Tan et al., 2017; Ye et al., 2011; Yuan et al., 2015; Ikehata et al., 2008). In situ isotopic compositions of sulfide minerals in hydrothermal systems can be efficiently determined by Laser Ablation Multi-Collector Inductively Coupled Plasma Mass Spectrometry (LA-MC-ICP-MS) (Bao et al., 2017; Chen et al., 2014b; Woodhead et al., 2009). In addition, several studies have explored the application of Sm-Nd isotopic system to determine the age of hydrothermal mineral deposition (e.g. Peng et al., 2003; Li et al., 2007; Barker et al., 2009; Su et al., 2009; Zhou et al., 2013; Zhang et al., 2015).

Since the Quemocuo deposit was newly discovered, few studies were conducted on this deposit. In this study, the Quemocuo deposit Pb-Zn deposit was chosen as the object, aiming to offer some new insights on the genesis of these Pb-Zn deposits in the Sanjiang Pb-Zn metallogenic belt. A combined study of the Sm-Nd isotopic dating, Sr isotopes and in situ S-Pb isotopic compositions were carried out in this contribution, with the attempts to constrain the ore-forming ages, source of metals and fluids for these Pb-Zn deposits and to propose a new integrated model. The conclusions are essential for understanding and prospecting of Pb-Zn mineralization in the Sanjinag Pb-Zn metallogenic belt, SW China.

2. Geological setting

2.1. Regional geology

The Tuotuohe area is located in western Sanjiang Pb-Zn metallogenic belt, northern Qiangtang Block, which is bounded by the Kekexili-Songpan-Ganzi block to the north, the Lhasa block to the south and the Tianshuihai block to the west (Fig. 1B). The strata exposed in the Sanjiang belt are mainly Paleozoic to Cenozoic (Fig. 2), consisting of Carboniferous clastic and carbonate rocks, Permian to Triassic carbonate, clastic, and volcanic rocks, Jurassic to Cretaceous limestone, subordinate volcanic rocks and evaporate, and Cenozoic carbonate, terrigenous clastic rocks with a few layers of gypsum and volcanic rocks (Zhu, 1999; Li et al., 2001, 2002; Song et al., 2015; Liu et al., 2015d). The Proterozoic metamorphic basement is exposed in Yushu, Changdu and Lanping area, consisting of gneiss, schist, migmatite, and limestone (He et al., 2013; Wang et al., 2018b; Xu et al., 2018; Pan et al., 2003).

The Sanjiang Belt has experienced several tectonic events, such as the Mesozoic-Cenozoic and Cenozoic collisional events, resulting in the formation of a series of large thrust and strike-slip fault systems and a series of Cenozoic sedimentary basins, respectively (Yin and Harrison, 2000; Hou et al., 2008; He et al., 2009). The development of basins was also associated with contemporaneous potassic magmatic activities (e.g. potassic volcanic and porphyritic potassium-rich intrusions; Deng et al., 2001; Zhao et al., 2004; Zhu et al., 2006; Zhao et al.,2007; Yang et al., 2008). The thrust and strike-slip fault systems were developed in the Sanjiang belt, which define the structural framework in this region (Li et al., 2006; Tang et al., 2006; He et al., 2009) and control magmatism, sedimentation and mineralization.

Multiple thrusting events have been recognized (Spurlin et al., 2005; Li et al., 2006; Tang et al., 2006). For example, Li et al. (2006, 2012) suggested that three thrust belts could be identified in Tuotuohe area, which are the Geraddong-Esuima thrust belt (root belt), the Quemocuo-Gaina fold-thrust belt (middle belt), and the Baqing-Wulwl thrust belt (front belt), and these thrust belts may form at 52–23 Ma. The carbonate-hosted Pb-Zn deposit in the Tuotuohe area mainly occurs in the middle zone and the front zone of the fold-thrust belt (Zhang,

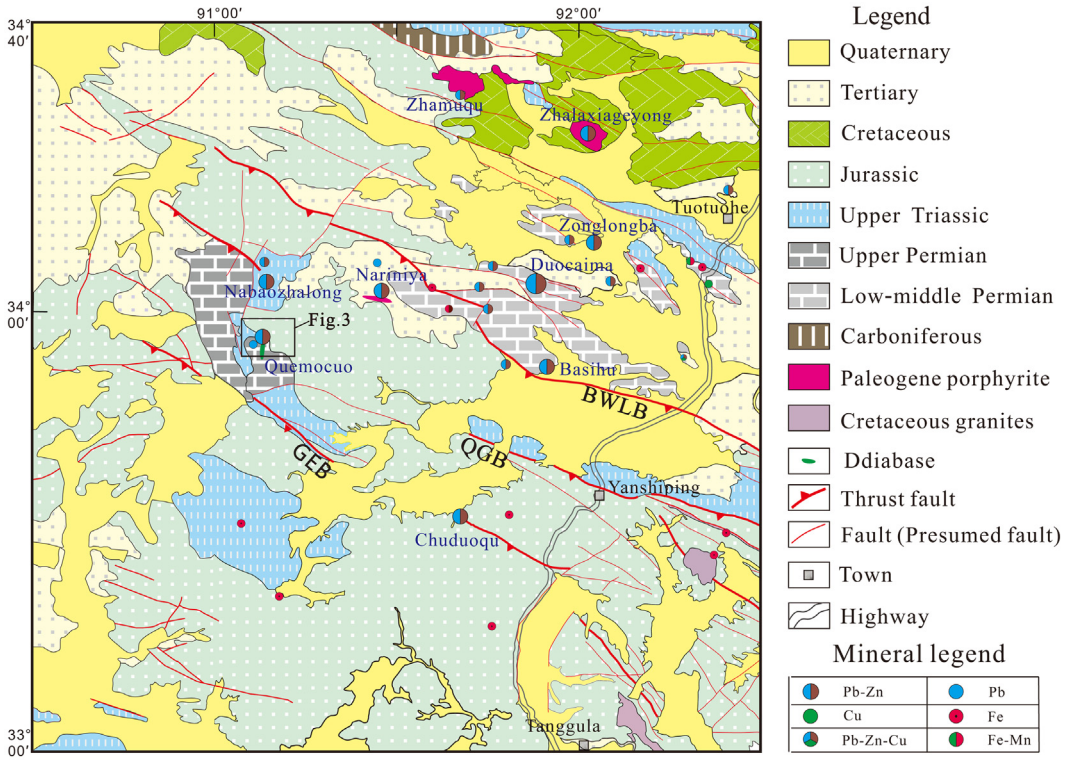

Fig. 2. The distribution of ore deposits, stratigraphy and regional structures in the Tuotuohe area. GEB, Geraddong-Esuima thrust belt; QGB, Quemocuo-Gaina fold-thrust belt; BWLB, Baqing-Wulwl thrust belt (Modified after Zhang, 2014; Li et al., 2012).

2014; Song et al., 2015). Qian (2014) suggests that the Pb-Zn mineralization in this area was associated with the Paleogene potassic magmatic activities (40–32 Ma). Also, these magmatic activities could be observed in Nariniya, Zhalaxiageyong, and Zhamuqu. In addition, Rb-Sr and Sm-Nd isotope geochronology studies indicate that the formation ages of several typical carbonate-hosted Pb-Zn deposits (e.g. Dongmozhazhua, Mohailaheng, Zhaofayong, and Lanping) in the Sanjiang Pb-Zn metallogenic belt range from 41 Ma to 29 Ma (Liu, 2012, Liu et al., 2015a,b,c,d,e, 2016). Therefore, it's suggested that the Pb-Zn mineralization in the Sanjiang Pb-Zn metallogenic belt occurred during the Cenozoic and is associated with thrust system and potassic magmatic rock, which is probably in response to the Indian-Eurasian continental collision.

2.2. Geology of the Quemocuo deposit

The Quemocuo deposit is located in the west of Duocaima deposit in Sanjiang Pb-Zn metallogenic belt, and the exposed strata mainly include Upper Permian Labuchari Formation and Quaternary (Fig. 3), which are composed of limestone and sandstone. Also, the diabase intruded Permian strata and is covered by the Quaternary.

The NW-trending fault is high angle thrust faults with dip angles between 55° and 85°, whereas the NE-trending faults are in parallel with normal faults in the Quemocuo deposit. Besides, almost all the fractures in the Quemocuo deposit have a close relationship with Pb-Zn ore bodies.

Six stratiform and veined ore bodies have been found in the Quemocuo deposit, and ore bodies are hosted in the Upper Permian Labuchari Formation limestone and are structurally controlled by the NE-trend normal faults (Figs. 3 and 4; Jia, 2014; Liu et al., 2015d). Ore bodies are NE-trend with dip angles of 45° to 75° (Figs. 3 and 4), the majority of ore bodies are 500 m-1500 m in length and 50 m-150 m in width. Reserves of these ore bodies are 7.1 Mt Pb + Zn (1.65 wt% to 7.17 wt% for Pb and 1.13 wt% to 5.7 wt% for Zn, average grade: 2.92 wt% Pb + Zn; Jia. 2014; Liu et al., 2015d).

The sulfide ores types of the Quemocuo deposit can be divided into brecciated (Fig. 5A and B), veined (Fig. 5C, H-I), massive (Fig. 5F) and disseminated (Fig. 5D-E, G) structures with anhedral, subhedral, euhedral or fine- to coarse-grained textures. Ore minerals include galena, sphalerite, pyrite, tetrahedrite, bournonite, marcasite, and cerussite. The gangue minerals comprise calcite, quartz, dolomite, and barite (Figs. 5–8).

Based on field investigation, microscope identification and scanning electron microscopy observations, the mineralization of the Quemocuo deposit can be divided into diagenetic, hydrothermal and oxidized phases. The main mineralization hydrothermal phase can be further subdivided into four stages (Fig. 8).

Stage I is the pyrite + calcite + quartz stage. Pyrite-I occurs as fine- to medium-grained and vein texture, which filled in limestone breccia (Figs. 5A-B, 6A-B and 7C). Minor fine-grained tetrahedrite is also present in this stage (Figs. 6C and 7C).

Stage II is the sphalerite + galena + pyrite + calcite + barite + quartz stage. This is the most important metallogenic stage, with a large number of disseminated and massive sphalerite and galena (Fig. 5D–G). Sphalerite-II is fine- to coarse-grained, coexisting with coarse-grained calcite-II, fine-grained galena-II, or fine- to coarse-grained pyrite-II (Figs. 5C-G and 6C-F). Most galena-II is medium- to coarse-grained, coexisting with coarse-grained calcite-II (Fig. 6E). Moreover, coarse-grained pyrite-II is cut by barite vein and coexist with quartz and calcite (Fig. 7D-E).

Stage III is the galena + sphalerite + pyrite + calcite + barite + quartz stage. A large number of vine-type galena is formed at this stage (Figs. 5H-I and 6G). Galena-III and pyrite-III are both fine- to medium-grained, replacing the early stage quartz and coexisting with barite (Figs. 6G-H and 7F). Minor disseminated sphalerite may be present in this stage. This is also an important mineralization stage.

Stage IV is the calcite + dolomite stage and is the final hydrothermal stage.

Wall rock alterations include silicification, baratization,

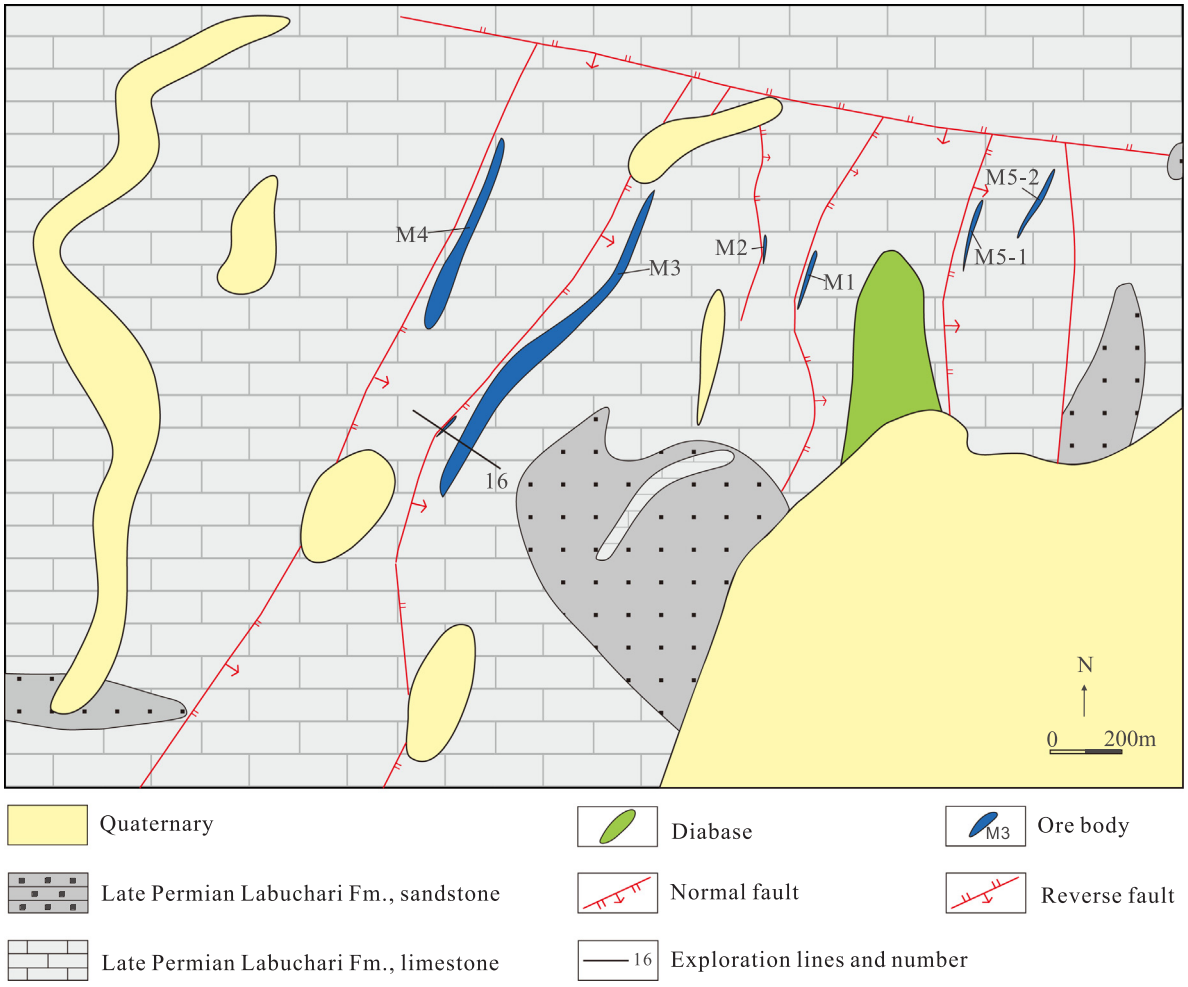

Fig. 3. Geological map of the Quemocuo Zn-Pb deposit, showing the lithologies, faults, exploration lines and ore bodies (Modified from Jia, 2014).

dolomitization, calcitization, and ferritization, of which calcitization and baratization are closely associated with the Pb-Zn mineralization.

3. Samples and analytical methods

3.1. Samples

Sulfide ores were collected from drill holes in the Quemocuo ore district. The collected samples are mainly disseminated and veined ores (Fig. 5 and Tables 1-4). Based on microscope observation and scanning electron microscopy (SEM) analysis, five polished thin sections (stage I-III) were selected for micro-scale LA-MC-ICP-MS in situ S and Pb isotope analysis. Furthermore, nine sphalerite samples (Stage II) and five calcite samples (Stage II) separates were handpicked from nine samples of disseminated sulfide ores under binocular for Rb-Sr and Sm-Nd isotope analysis.

3.2. Analytical methods

3.2.1. Sm-Nd isotope analysis

The five samples of calcite were analyzed on an inductively coupled plasma mass spectrometry at the Center of Modern Analysis, Nanjing University, China. The analyses of Sm-Nd isotopic compositions of calcites followed the procedure described by Wang et al. (2007) and Li et al. (2007). The ratio of $^{143}Nd/^{144}Nd$ of American La Jolla isotopic standard sample was tested to be in the range of 0.511860 ± 8 (2σ) and the ratio of $^{143}Nd/^{144}Nd$ of the American BCR-1 isotopic standard sample was tested to be in the range of 0.512642 ± 8 (2σ). To normalize all of Nd ratios, the $^{146}Nd/^{144}Nd$ = 0.7219 was adopted. After calculation, the analytical errors in $^{147}Sm/^{144}Nd$ (2σ) are within ± 0.2%. The Sm-Nd isochronic age was calculated by ISOPLOT 3.0 (Ludwig, 2003).

3.2.2. In situ S isotope analysis

Sulfur isotope analysis were performed by using a Nu 1700 MC-ICP-MS system, equipped with sixteen Faraday cups and three ion counters at the State Key Laboratory of Continental Dynamics in Northwest University, Xi'an, China. The mass separation was calculated as 0.3333 in the analyses. The Nu 1700 system was able to completely separate the interference peaks for 32 and 33 S in the medium (resolution power = 10,000) and high (resolution power = 18,000) resolution modes, respectively. The determination of unmixed sulfur peaks ensures the stability and accuracy of the results. A detailed description of the measuring procedures is available in Bao et al. (2017); Chen et al. (2017).

3.2.3. In situ Pb isotope analysis

High-precision in situ lead isotope analyses of pyrite and galena were conducted on thick polished sections (50–100 μm in thickness), using a Nu Plasma™ multi-collector ICPMS with a 193 nm excimer laser denudation system (RESOlution M-50, ASI) at the State Key Laboratory of Continental Dynamics in Northwest University, Xi'an, China. The interference of ^{204}Hg on ^{204}Pb was calculated by using the natural abundance ratio of $^{204}Hg/^{202}Hg$ = 0.229883 (^{202}Hg = 0.29863 and ^{204}Hg = 0.06865) and the adjustment for instrumental mass fractionation was monitored by the $^{205}Tl/^{203}Tl$ ratio. NIST SRM 610 was used

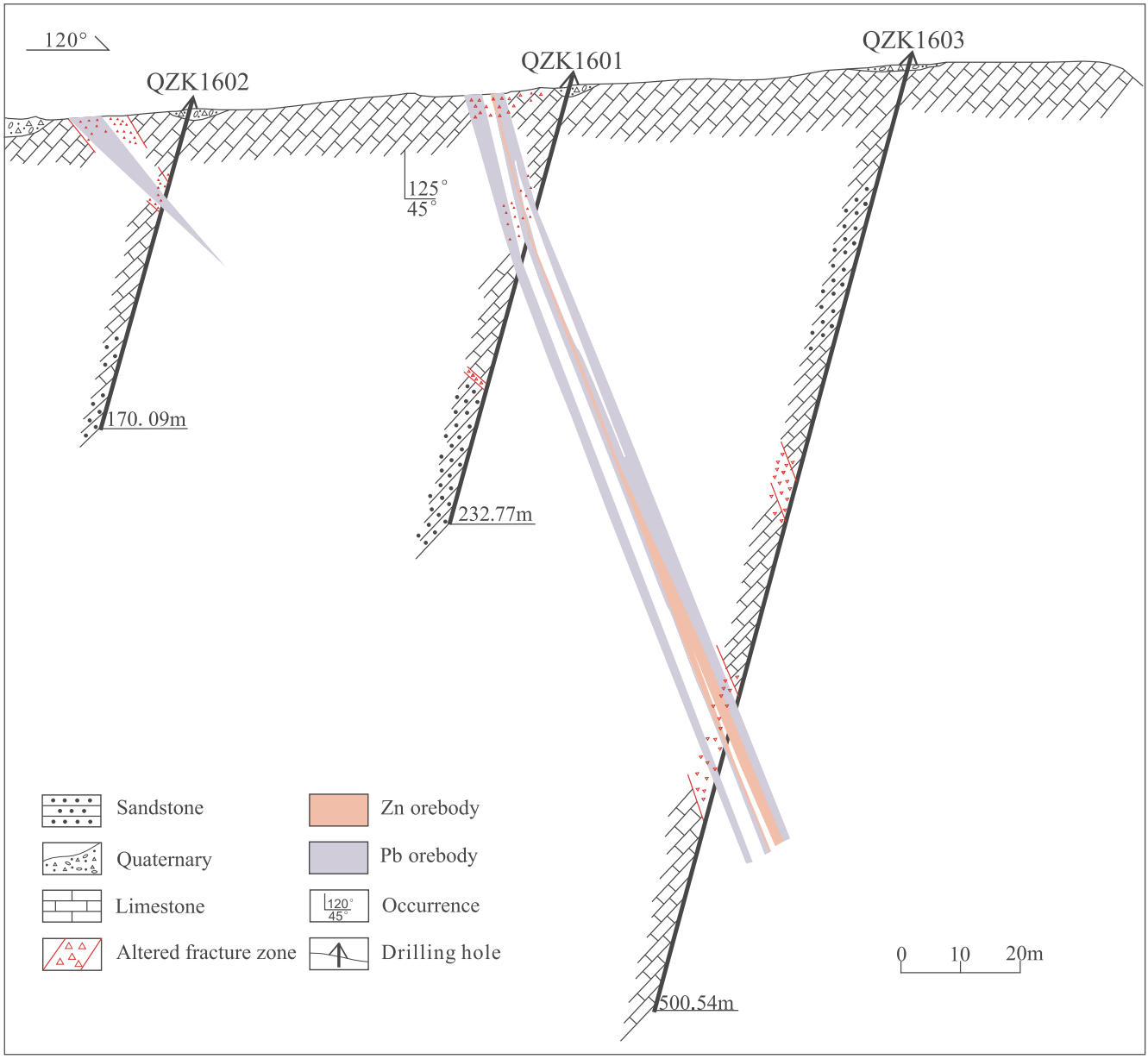

Fig. 4. Exploration lines K16 cross-sections of the Quemocuo Zn-Pb deposit showing the drilling, ore bodies and host rock lithologies (Modified from Jia, 2014). The location of this cross-section is shown in Fig. 3.

as equality control sample (Yuan et al., 2013) and the obtained average values of Pb isotopic compositions of NIST SRM 610 in this study are: $^{208}Pb/^{204}Pb = 36.981 \pm 0.007$, $^{207}Pb/^{204}Pb = 15.515 \pm 0.003$ and $^{206}Pb/^{204}Pb = 17.052 \pm 0.003$ (1σ). The precision of Pb isotope analysis are within the range of ± 0.06%. A detailed description of the measuring procedures is available in Bao et al. (2017); Chen et al. (2014b); Yuan et al. (2015).

3.2.4. Rb-Sr isotope analysis

The Center of Modern Analysis (Nanjing University, Nanjing, China) measured the Rb-Sr isotope and analyzed on a mass spectrometer with five collectors, model VG-354. Reproducibility and accuracy of the Sr-isotope assay results were periodically checked by both running the Standard Reference Material NBS 987 and the Laboratory Standard La Jolla. The mean value of $^{87}Sr/^{86}Sr$ is equal to 0.710236 ± 0.000007 and it is used for correction of instrumental fractionation, the ratio of $^{87}Sr/^{86}Sr$ is normalized to $^{86}Sr/^{88}Sr = 0.1194$. Details of the chemical separation and mass spectrometric procedures are described by Wang et al., (2007) and Hu et al. (2015). The age of Rb-Sr isochronic was calculated using the ISOPLOT 3.0 computer program (Ludwig, 2003).

4. Analytical results

4.1. Sm-Nd isochronic age

Sm-Nd isochronic age for five calcite samples in stage II and their isotopic compositions are presented in Table 1, yielding Sm and Nd concentrations of 0.1023–0.3809 × 10^{-6} and 0.3317–0.9498 × 10^{-6}, respectively. The $^{143}Nd/^{144}Nd$ values vary from 0.512342 to 0.512539. The $^{143}Sm/^{144}Nd$ values range from 0.0653 to 0.9807, and the significant variation and range of these values suggest that a precise Sm-Nd isochronic age could be obtained for these samples. On the $^{147}Sm/^{144}Nd$-$^{143}Nd/^{144}Nd$ plots (Fig. 9A), the straight line can be interpreted in two different ways, that is, a true isochron or mixing between two end-members with different $^{147}Sm/^{144}Nd$ and $^{143}Nd/^{144}Nd$ ratios (Jiang et al., 2000; Peng et al.,2003; Su et al., 2009). However,

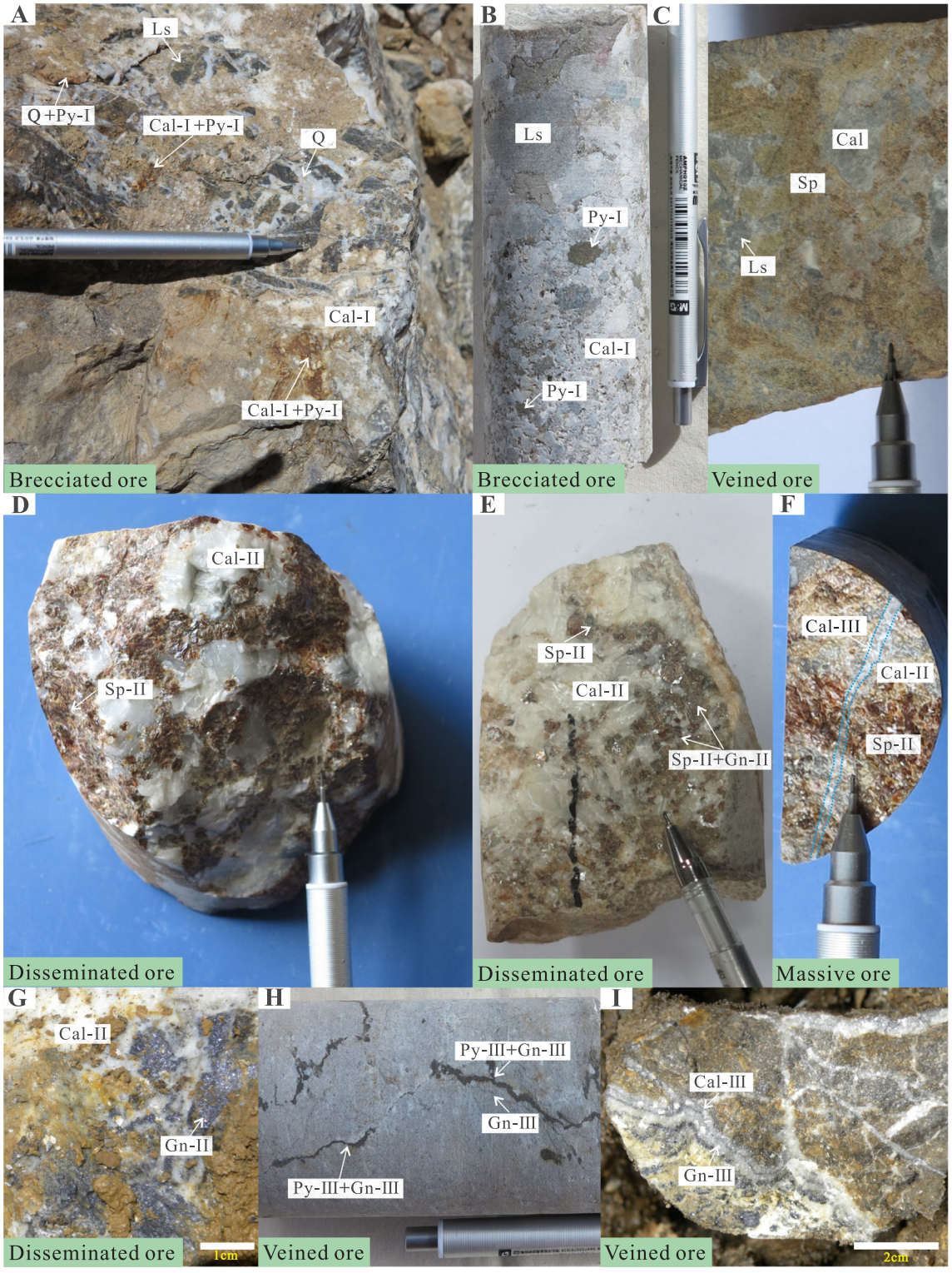

Fig. 5. Photographs of hand specimens in the Quemocuo deposit. A-B: brecciated ore. limestone (Ls) breccia is cemented by quartz (Q), calcite-I (Cal-I) and pyrite-I (Py-I); C: veined ore, sphalerite (Sp) + calcite vein is filled in Ls breccia; D-E: disseminated ore, Sp-II and galena-II (Gn-II) coexists with Cal-II; F: massive ore, Sp-II + Gn-II is cut by Cal-III vein; G: disseminated ore, Gn-II is cemented by Cal-II; H-I: veined ore, Gn-III + Py-III + Cal-III vein is filled in Ls.

the lack of correlation between 1/Nd and $^{143}Nd/^{144}Nd$ in the samples rules out the possibility of two-component mixing (Fig. 9B). These samples yielded the Sm-Nd isochronic age of 34.3 ± 2.2 Ma with the mean square of weighted deviates (MSWD) of 7.1, and an initial $^{143}Nd/^{144}Nd$ ratio is 0.512318 ± 7 (Fig. 9A).

4.2. *In situ S isotopic compositions*

In situ sulfur isotopic ratios for four sulfide samples, together with previously published bulk S isotopic data (Jia, 2014), are listed in Table 2 and are shown in (Fig. 10). The pyrite samples in stage I have low $\delta^{34}S_{CDT}$ values, varying from −29.5‰ to −26.5‰. The $\delta^{34}S_{CDT}$

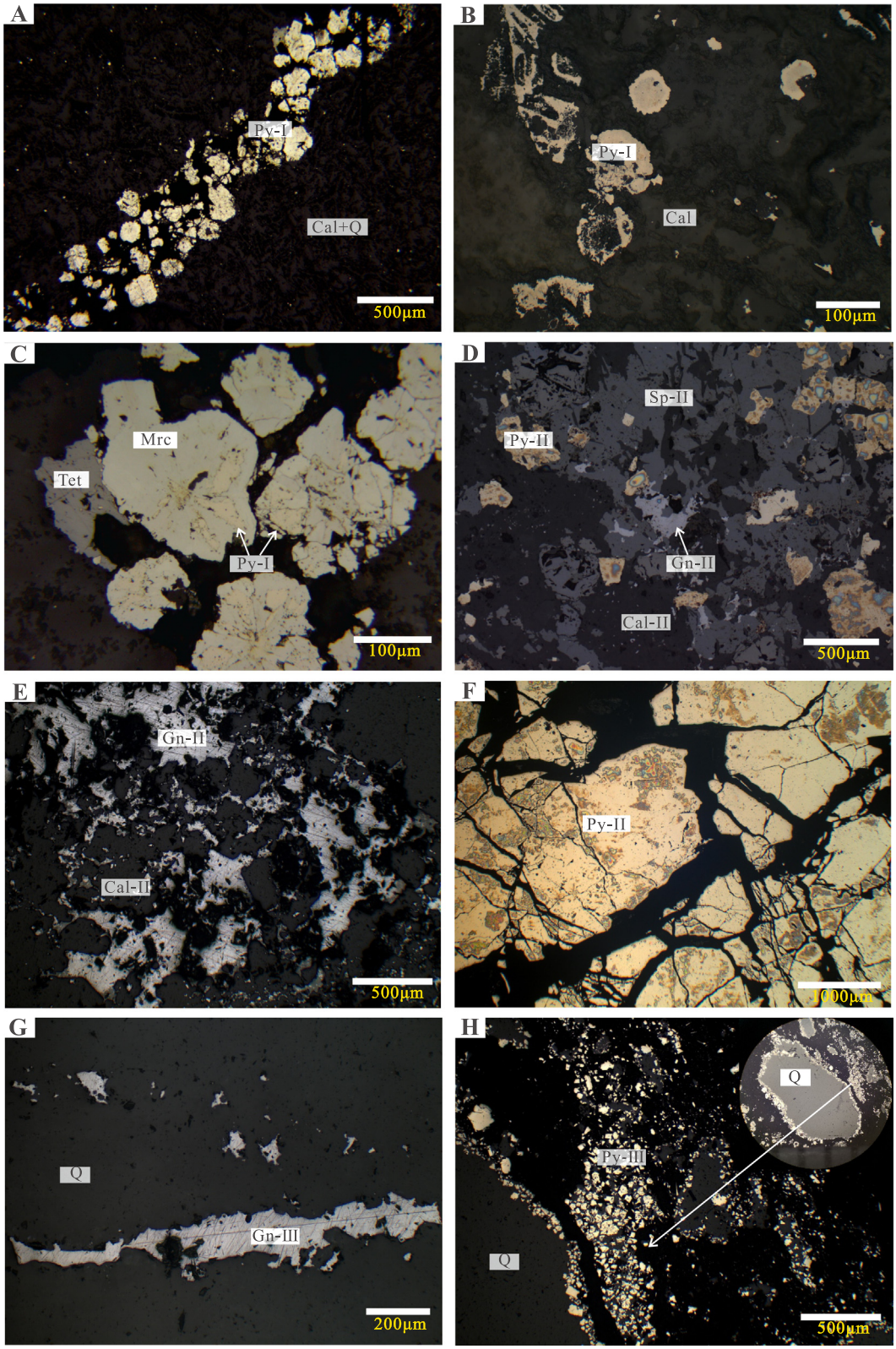

Fig. 6. Microscopic texture and structural features of minerals in the Quemocuo deposit. A-B: veined or fine- to medium-grained Py-I is enclosed by calcite (Cal) and quartz (Q); C: fine-grained pyrite-I (Py-I) and marcasite (Mrc) coexist with fine-grained tetrahedrite (Tet); D: fine- to coarse-grained sphalerite-II (Sp-II), fine- to coarse-grained Py-II and fine-grained galena-II (Gn-II) coexists with coarse-grained calcite-II (Cal-II); E; medium- to coarse-grained (Gn-II) coexists with coarse-grained calcite-II (Cal-II); F: fractured coarse-grained Py-II; G: fine-grained Gn-III occurs as vein; H: quartz grain is replaced by fine-grained Py-III, forming a ring shape in fracture.

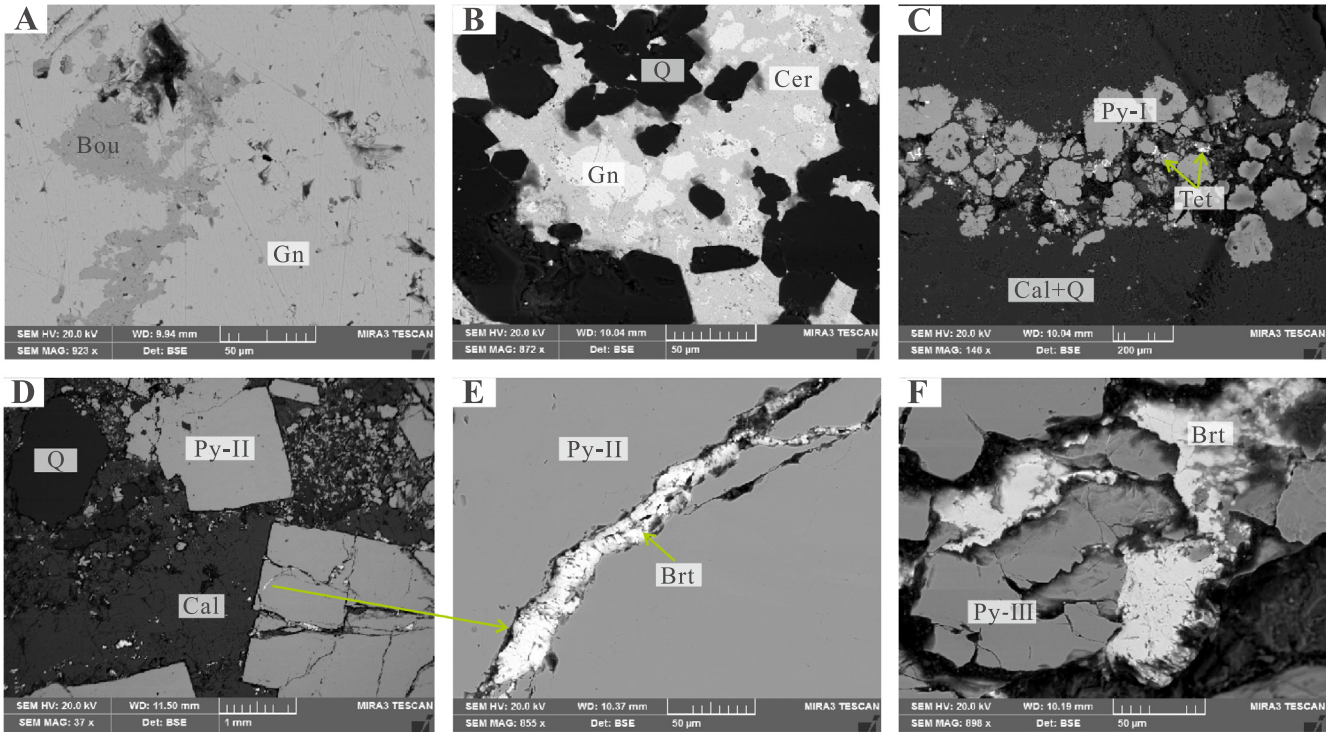

Fig. 7. Textures and structures of hydrothermal minerals in the Quemocuo deposit under the scanning electron microscope (SEM). A: galena (Gn) coexists with bournonite (Bou); B: galena is replaced by cerussite (Cer) and coexists with quartz (Q); C: galena + tetrahedrite (Tet) vein is filled in calcite (Cal) and quartz (Q); D-E: pyrite-II (Py-II) is cut by barite (Brt) vein and coexists with quartz and calcite; F: Py-III coexists with barite (Brt).

value of the pyrite samples in stage II is −4.7‰, and $\delta^{34}S_{CDT}$ values varying from +4.7‰ to +5.5‰ in stage III. The galena samples in stage II have $\delta^{34}S_{CDT}$ values of +4.0‰ to +6.0‰, and the $\delta^{34}S_{CDT}$ value show a range from +1.7‰ to 6.9‰ in stage III. For the sulfur isotopic compositions, the pyrite samples in different stages have significant variation, but the galena samples have few differences. On the other hand, compared with bulk $\delta^{34}S$ values of sulfides (Jia, 2014), in situ S isotopic data has a much wider range (Fig. 10).

4.3. In situ Pb isotopic ratios

In situ lead isotopic compositions of sulfides are listed in Table 3 and shown in (Figs. 11 and 12). Ten pyrite samples in stage I have $^{206}Pb/^{204}Pb$, $^{207}Pb/^{204}$ Pb and $^{208}Pb/^{204}Pb$ ratios ranging from 18.684 to 18.826 (average: 18.798), 15.673 to 15.702 (average: 15.682) and 38.877 to 39.112 (average: 39.056), respectively. Two pyrite samples from stage II show $^{206}Pb/^{204}Pb$, $^{207}Pb/^{204}Pb$ and $^{208}Pb/^{204}Pb$ ratios ranging from 18.686 to 18.750 (average: 18.718), 15.630 to 15.662 (average: 15.646) and 38.775 to 38.902 (average: 38.839), respectively. Eleven pyrite samples from stage III have ^{206} Pb/^{204}Pb, $^{207}Pb/^{204}Pb$ and $^{208}Pb/^{204}Pb$ ratios ranging from 18.547 to 19.202 (average: 18.849), 15.539 to 15.750 (average: 15.646) and 38.582 to 39.162 (average: 38.922), respectively. Twenty-one galena samples from stage II show their Pb isotopic compositions ranging from 18.589 to 18.598 (average: 18.593) for ^{206} Pb/^{204}Pb, from 15.654 to 15.663 (average: 15.658) for $^{207}Pb/^{204}Pb$, and from 38.690 to 38.714 (average: 38.699) for $^{208}Pb/^{204}Pb$, respectively. The galena samples in stage III have $^{206}Pb/^{204}Pb$, $^{207}Pb/^{204}Pb$ and $^{208}Pb/^{204}Pb$ ratios ranging from 18.593 to 18.768 (average: 18.605), 15.660 to 15.689 (average: 15.665) and 38.705 to 39.039 (average: 38.729), respectively.

4.4. Rb-Sr isochronic ratios

The Rb and Sr concentrations and isotopic results of sphalerite from the Quemocuo Pb-Zn deposit are listed in Table 4. The sphalerite samples have Rb and Sr contents of 0.1583–0.9521 × 10^{-6} and 0.4305–2.7430 × 10^{-6}, respectively. The values of $^{87}Sr/^{86}Sr$ range from 0.708482 to 0.711732, with an average of 0.70939, and the ratios

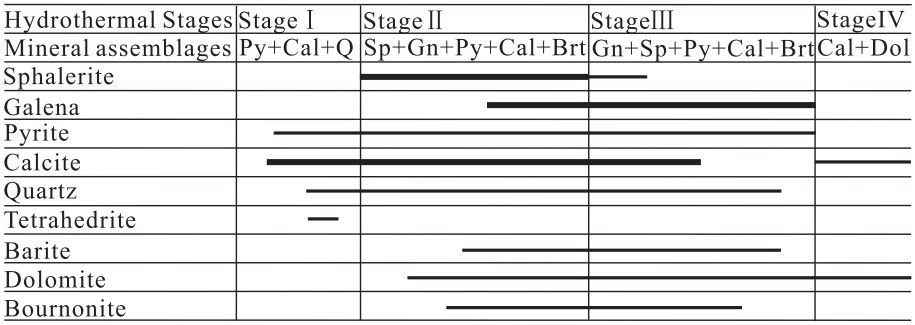

Fig. 8. Mineral paragenesis of the Quemocuo deposit.

Table 1
Calcite Sm-Nd isotopes compositions of the Quemocuo Pb-Zn deposit.

Sample No.	Mineral	$Sm/10^{-6}$	$Nd/10^{-6}$	$^{147}Sm/^{144}Nd$	$^{143}Nd/^{144}Nd$	± 2σ
ZK701-ABb1	Stage II Calcite	0.1897	0.8229	0.1398	0.512351	0.000006
ZK701-Bb1	Stage II Calcite	0.1923	0.5425	0.2187	0.512362	0.000007
ZK701-ABb8	Stage II Calcite	0.3809	0.3317	0.9807	0.512539	0.000009
ZK701-Bb4	Stage II Calcite	0.1023	0.9498	0.0653	0.512335	0.000009
ZK701-ABb4	Stage II Calcite	0.1247	0.7219	0.1042	0.512342	0.000008

of $^{87}Rb/^{86}Sr$ isotopes have a wide range from 0.1059 to 6.5260. Affected by some factors, the sphalerite Rb-Sr isotope system did not yield ideal isochronic age, but the Sm-Nd dating of hydrothermal calcite suggested that the Quemocuo deposit was formed at 34 Ma. Then, this age was used to correct the initial Sr isotopes. In this manner, we obtain the $^{87}Sr/^{86}Sr_{34\ Ma}$ of all sphalerite separates, which have a range from 0.7085 to 0.7117, with an average of 0.7094 (Fig. 13). Such initial Sr isotope signatures indicate that sphalerite is rich in radiogenic Sr isotopes.

5. Discussion

5.1. Timing of Pb-Zn mineralization

Although dating of hydrothermal mineral deposits is often difficult, the age is critical for understanding the relationship between the timing of mineralization and other geological events. The Sm-Nd isotopic compositions of calcium-bearing minerals in ore-forming stage, such as calcite and fluorite, have been widely used to determine the formation ages of hydrothermal deposits (e.g. Chesley et al., 1994; Penget al., 2003; Muchez et al., 2005; Uysal et al., 2007; Su et al., 2009; Dill et al., 2011; Zhang et al., 2015). Homogeneous Sm-Nd isotopic compositions for a single set of samples are a prerequisite for obtaining reliable Sm-Nd ages.

In this study, the calcite has homogeneous initial $^{143}Nd/^{144}Nd$ ratios ranging from 0.512342 to 0.512539. The lack of covariance between 1/Nd and $^{143}Nd/^{144}Nd$ (Fig. 9B) for these calcites indicates that the isochronic age is not a pseudo-isochronic age and has geological mean (Jiang et al., 2000; Peng et al., 2003; Li et al., 2007; Barker et al., 2009; Su et al., 2009; Zhou et al., 2013). Therefore, the Sm-Nd isochronic age of 34.3 ± 2.2 Ma for five calcite samples in the main metallogenic stage from the Quemocuo deposit is considered to be reliable (Fig. 9A), and this age is interpreted to reflect the timing of the Pb-Zn mineralization. The Sm-Nd isochoric age is similar to the calcite Sm-Nd isochoric ages of the Duocaima Pb-Zn deposit (35.3 ± 1.2 Ma; Liu, 2012). In addition, previous studies reported that the Rb-Sr sphalerite dating and Sm-Nd fluorite dating yield ages of 35–32 Ma for the Pb-Zn mineralization in the Mohailaheng and Dongmozhazhua Pb-Zn deposits from Yushu area (Tian et al., 2014), the hydrothermal calcite from the Zhaofayong Pb-Zn deposit in Changdu area yields the Sm-Nd isochoric age of 41–38 Ma (Liu et al., 2016), and the Rb-Sr dating of sphalerite and Sm-Nd dating of calcite yield ages of 30–29 Ma for the Baiyangping Pb-Zn Ore Cluster in Lanping area (Wang et al., 2011). Hence, we suggest that these deposits formed simultaneously, and the predominant Pb-Zn mineralization event in the Sanjiang province occurred at 41–29 Ma and is related to the continental collision of the Indian-Eurasian (Hou et al., 2008; Hou and Zhang, 2015; Liu et al., 2011, 2015e, 2016, 2017; Song et al., 2015, 2017, 2019; Tian et al., 2014; L. J. Wang et al., 2018; Wang et al., 2011; X. H. Wang et al., 2018; Liu et al., 2015d; Liu, 2012).

5.2. Possible sulfur sources

The sulfur isotopic compositions of sulfur-bearing minerals are mostly affected by source and fractionation (Ohmoto and Goldhaber, 1997; Hoefs, 2015; Seal, 2006). Hence, the source of sulfur and the

Table 2
In situ and bulk sulfur isotopic compositions from the Quemocuo deposit.

No.	Structure	Mineral	Stage	$\delta^{34}S_{V\text{-}CDT}$(‰)	Source
ZK801Bb2-Py1	Veined ores	Pyrite	Stage I	−29.5	This paper (In situ S isotopic data)
ZK801Bb2-Py2	Veined ores	Pyrite	Stage I	−28.7	
ZK801Bb2-Py3	Veined ores	Pyrite	Stage I	−29.3	
ZK801Bb2-Py4	Veined ores	Pyrite	Stage I	−26.7	
ZK801Bb2-Py5	Veined ores	Pyrite	Stage I	−28.5	
ZK701Bb2-Py1	Disseminated ores	Pyrite	Stage II	−4.7	
ZK701Bb2-Py2	Veined ores	Pyrite	Stage III	4.7	
ZK801Bb1-Py1	Veined ores	Pyrite	Stage III	5.4	
ZK801Bb1-Py2	Veined ores	Pyrite	Stage III	5.5	
D027-Gn1	Disseminated ores	Galena	Stage II	5.3	
D027-Gn2	Disseminated ores	Galena	Stage II	4.0	
D027-Gn3	Disseminated ores	Galena	Stage II	6.0	
D028-Gn1	Veined ores	Galena	Stage III	6.6	
D028-Gn2	Veined ores	Galena	Stage III	6.0	
D028-Gn3	Veined ores	Galena	Stage III	6.9	
D028-Gn4	Veined ores	Galena	Stage III	4.5	
D028-Gn5	Veined ores	Galena	Stage III	5.1	
D028-Gn6	Veined ores	Galena	Stage III	1.7	
D028-Gn7	Veined ores	Galena	Stage III	5.6	
D028-Gn8	Veined ores	Galena	Stage III	4.3	
QMC-TC1-B14-2				2.4	Jia, 2014 (Bulk S isotopic data)
QMC-3#-TC5-W4				3.4	
QMC-3#-TC9-B1				2.2	
QMC-TC1-B11-1				2.3	
QMC-TC1-B15				3.3	
QMC-TC1-W4				2.9	

Table 3
In situ and bulk Pb isotopic ratios of sulfides from the Quemocuo deposit.

No.	Structure	Mineral	Stage	$^{206}Pb/^{204}Pb$	1 s	$^{207}Pb/^{204}Pb$	1 s	$^{208}Pb/^{204}Pb$	1 s	Source
D027-Gn3	Disseminated ores	Galena	Stage II	18.594	0.003	15.659	0.003	38.704	0.009	This paper (In situ Pb isotopic data)
D027- Gn4		Galena	Stage II	18.597	0.003	15.659	0.003	38.702	0.008	
D027- Gn5		Galena	Stage II	18.591	0.003	15.656	0.003	38.694	0.009	
D027- Gn6		Galena	Stage II	18.594	0.003	15.658	0.003	38.697	0.010	
D027- Gn7		Galena	Stage II	18.595	0.003	15.659	0.003	38.702	0.009	
D027- Gn9		Galena	Stage II	18.594	0.003	15.661	0.003	38.708	0.008	
D027- Gn10		Galena	Stage II	18.591	0.003	15.657	0.003	38.690	0.010	
D027- Gn11		Galena	Stage II	18.591	0.003	15.658	0.004	38.697	0.010	
D027- Gn12		Galena	Stage II	18.590	0.004	15.657	0.004	38.698	0.011	
D027- Gn13		Galena	Stage II	18.591	0.003	15.657	0.003	38.697	0.009	
D027- Gn14		Galena	Stage II	18.598	0.003	15.663	0.003	38.714	0.009	
D027- Gn15		Galena	Stage II	18.590	0.003	15.656	0.003	38.693	0.009	
D027- Gn16		Galena	Stage II	18.589	0.002	15.656	0.003	38.691	0.008	
D027- Gn17		Galena	Stage II	18.598	0.003	15.658	0.003	38.704	0.008	
D027- Gn18		Galena	Stage II	18.596	0.003	15.659	0.003	38.702	0.009	
D027- Gn19		Galena	Stage II	18.593	0.003	15.659	0.003	38.702	0.010	
D027- Gn20		Galena	Stage II	18.591	0.003	15.655	0.003	38.691	0.009	
D027- Gn21		Galena	Stage II	18.592	0.003	15.659	0.003	38.697	0.008	
D027- Gn22		Galena	Stage II	18.592	0.002	15.659	0.003	38.700	0.008	
D027- Gn23		Galena	Stage II	18.597	0.002	15.658	0.002	38.697	0.007	
D027- Gn24		Galena	Stage II	18.595	0.003	15.658	0.003	38.700	0.008	
D028Bb1-Gn1	Veined ores	Galena	Stage III	18.605	0.001	15.669	0.001	38.729	0.003	
D028Bb1-Gn2		Galena	Stage III	18.599	0.001	15.665	0.001	38.718	0.003	
D028Bb1-Gn3		Galena	Stage III	18.597	0.001	15.663	0.001	38.714	0.003	
D028Bb1-Gn4		Galena	Stage III	18.598	0.001	15.664	0.001	38.713	0.003	
D028Bb1-Gn5		Galena	Stage III	18.598	0.001	15.663	0.001	38.711	0.003	
D028Bb1-Gn6		Galena	Stage III	18.596	0.001	15.662	0.001	38.709	0.003	
D028Bb1-Gn7		Galena	Stage III	18.597	0.001	15.660	0.001	38.705	0.003	
D028Bb1-Gn8		Galena	Stage III	18.599	0.001	15.662	0.001	38.713	0.003	
D028Bb1-Gn9		Galena	Stage III	18.604	0.001	15.666	0.001	38.725	0.004	
D028Bb1-Gn10		Galena	Stage III	18.596	0.002	15.662	0.002	38.709	0.004	
D028Bb1-Gn16		Galena	Stage III	18.595	0.001	15.665	0.001	38.715	0.003	
D028Bb1-Gn11		Galena	Stage III	18.595	0.001	15.661	0.001	38.709	0.003	
D028Bb1-Gn12		Galena	Stage III	18.593	0.001	15.662	0.001	38.711	0.003	
D028Bb1-Gn13		Galena	Stage III	18.606	0.001	15.664	0.001	38.718	0.003	
D028Bb1-Gn14		Galena	Stage III	18.600	0.001	15.666	0.001	38.717	0.004	
D028Bb1-Gn15		Galena	Stage III	18.599	0.002	15.666	0.001	38.722	0.004	
D028Bb1-Gn17		Galena	Stage III	18.598	0.002	15.666	0.002	38.721	0.004	
D028Bb1-Gn18		Galena	Stage III	18.595	0.002	15.666	0.002	38.719	0.004	
D028Bb1-Gn19		Galena	Stage III	18.598	0.001	15.663	0.001	38.714	0.004	
D028Bb1-Gn20		Galena	Stage III	18.599	0.002	15.665	0.001	38.719	0.004	
D028Bb1-Gn21		Galena	Stage III	18.597	0.001	15.666	0.001	38.722	0.004	
D028Bb1-Gn22		Galena	Stage III	18.604	0.002	15.666	0.002	38.728	0.005	
D028Bb1-Gn23		Galena	Stage III	18.598	0.002	15.666	0.002	38.728	0.005	
D028Bb1-Gn24		Galena	Stage III	18.594	0.001	15.660	0.001	38.706	0.003	
D028Bb1-Gn25		Galena	Stage III	18.768	0.001	15.689	0.001	39.039	0.002	
ZK801Bb1-Py3	Veined ores	Pyrite	Stage III	18.826	0.005	15.691	0.004	39.103	0.010	
ZK801Bb1-Py6		Pyrite	Stage III	18.820	0.008	15.702	0.006	39.112	0.017	
ZK801Bb1-Py8		Pyrite	Stage III	18.795	0.008	15.679	0.007	39.058	0.017	
ZK801Bb1-Py41		Pyrite	Stage III	18.811	0.003	15.680	0.003	39.074	0.007	
ZK801Bb1-Py42		Pyrite	Stage III	18.804	0.004	15.674	0.003	39.058	0.009	
ZK801Bb1-Py43		Pyrite	Stage III	18.806	0.003	15.672	0.002	39.053	0.006	
ZK801Bb1-Py44		Pyrite	Stage III	18.814	0.002	15.678	0.002	39.075	0.004	
ZK801Bb1-Py45		Pyrite	Stage III	18.804	0.010	15.677	0.008	39.055	0.020	
ZK801Bb1-Py46		Pyrite	Stage III	18.821	0.006	15.696	0.005	39.097	0.012	
ZK801Bb1-Py47		Pyrite	Stage III	18.684	0.015	15.679	0.012	38.877	0.031	
ZK701Bb2-Py21	Disseminated ores	Pyrite	Stage II	18.686	0.036	15.630	0.031	38.775	0.077	
ZK701Bb2-Py51		Pyrite	Stage II	18.750	0.022	15.662	0.019	38.902	0.048	
ZK801Bb2-Py1	Veined ores	Pyrite	Stage I	18.976	0.004	15.686	0.003	39.116	0.008	
ZK801Bb2-Py2		Pyrite	Stage I	18.800	0.005	15.520	0.005	38.749	0.012	
ZK801Bb2-Py41		Pyrite	Stage I	18.767	0.003	15.701	0.002	38.977	0.005	
ZK801Bb2-Py42		Pyrite	Stage I	18.938	0.004	15.668	0.003	38.981	0.007	
ZK801Bb2-Py47		Pyrite	Stage I	18.822	0.001	15.646	0.001	38.912	0.003	
ZK801Bb2-Py7		Pyrite	Stage I	18.581	0.011	15.582	0.009	38.730	0.023	
ZK801Bb2-Py9		Pyrite	Stage I	19.202	0.005	15.717	0.004	39.162	0.009	
ZK801Bb2-Py10		Pyrite	Stage I	19.028	0.006	15.695	0.005	39.046	0.013	
ZK801Bb2-Py11		Pyrite	Stage I	18.846	0.014	15.750	0.011	39.022	0.027	
ZK801Bb2-Py14		Pyrite	Stage I	18.547	0.013	15.539	0.011	38.582	0.027	
ZK801Bb2-Py15		Pyrite	Stage I	18.829	0.007	15.601	0.007	38.869	0.017	
QMC-TC1-B14-2		Ore		18.579		15.645		38.650		Jia,2014 (Bulk Pb isotopic data)
QMC-3#-TC5-W4		Ore		18.596		15.665		38.715		
QMC-3#-TC9-B1		Ore		18.598		15.664		38.714		
QMC-TC1-B11-1		Ore		18.615		15.680		38.764		
QMC-TC1-B15		Ore		18.584		15.649		38.660		
QMC-TC1-W4		Ore		18.585		15.647		38.656		

Table 4
Sphalerite Rb-Sr isotopes compositions of the Quemocuo Pb-Zn deposit.

Sample No.	$Rb/10^{-6}$	$Sr/10^{-6}$	$^{87}Rb/^{86}Sr$	$^{87}Sr/^{86}Sr$	± 2σ	$^{87}Sr/^{86}Sr_{34Ma}$	Source
ZK701-ABb1	0.1702	2.743	0.1837	0.708641	0.000008	0.708641	This paper
ZK701-Bb1	0.1583	4.408	0.1059	0.708482	0.000009	0.708482	
ZK701-ABb8	0.9521	0.4305	6.526	0.711723	0.000007	0.711723	
ZK701-BBb9	0.8309	0.7186	3.408	0.710104	0.000009	0.710104	
ZK701-CBb1	0.5703	0.9659	1.745	0.709452	0.000006	0.709452	
ZK701-Bb6	0.6134	0.8332	2.169	0.709551	0.000009	0.709551	
ZK701-Bb4	0.4572	1.386	0.9731	0.709062	0.000008	0.709062	
ZK701-ABb4	0.3741	1.745	0.6315	0.708759	0.000009	0.708759	
D046-Bb1	0.1984	1.98	0.2947	0.708743	0.000008	0.708743	

$(^{87}Sr/^{86}Sr)t = {}^{87}Sr/^{86}Sr - {}^{87}Sr/^{87}Rb\ (e^{\lambda t}-1)$, $\lambda_{Rb} = 1.41 \times 10^{-11} t^{-1}$, t = 34 Ma.

evolution of ore-forming fluids could be revealed by sulfur isotopes.

The sulfur isotopic composition of pyrite formed in stage I (Py-I) is ranging from −29.5‰ to −26.7‰ (Fig. 10 and Table 2), which is significantly lower than that of the mantle-derived sulfur (−3 to +3‰: Chaussidon et al., 1989). Such a notably negative $\delta^{34}S$ value of pyrite can be achieved by bacterial sulfate reduction (BSR) of seawater/sulfate minerals (Goldhaber and Kaplan, 1975; Basuki et al., 2008). The hosting rocks from the Quemocuo Pb-Zn deposit formed in the Permian period and the $\delta^{34}S$ value of the seawater in the same period are about +11‰ to +16‰ (Claypool et al., 1980). Therefore, the fractionation of sulfur isotopic compositions between seawater and pyrite (Py-I) is about + 40‰. Such large sulfur isotopic fractionation can be caused by bacterial sulfate reduction (BSR) of seawater/sulfate minerals. We propose that the sulfur source of the sulfides in stage I is mainly from the marine sulfate by BSR.

The $\delta^{34}S$ value of pyrite formed in stage II (Py-II) is −4.7‰ and that of galena (Gn-II) is +4.0‰ to +6.0‰ (Fig. 10 and Table 2). Considering that the sulfur isotopic fractionation between galena (Gn-II) and Permian seawater is about 5‰-12‰, the $\delta^{34}S$ value of the thermochemical sulfate reduction (TSR) of seawater or sulfate minerals can better match the sulfur isotopic compositions of galena (Gn-II) (Ohmoto, 1986; Ohmoto and Goldhaber, 1997; Worden et al., 1995; Zhu et al., 2014). As for the pyrite (Py-II) with relatively negative $\delta^{34}S$ value (−4.7‰), it may be modified by some residual pyrites in stage I. In this way, sulfur isotopic compositions of fluid in stage II can down to a negative value locally. Pyrite (Py-III) and galena (Gn-III) formed in stage III have moderately positive $\delta^{34}S$ value with a range of +4.7‰ to +5.5‰ and +1.7‰ to +6.9‰, respectively (Fig. 10 and Table 2). The sulfur source of stage III may be the same as that of stage II, namely, the sulfur is mainly from the TSR of seawater/sulfate. It is worth noting that one galena analysis has yielded low $\delta^{34}S_{CDT}$ values (1.7‰), similar to that of mantle-derived sulfur (Chaussidon et al., 1989). The diabase dikes are exposed in the Quemocuo mining area, and the volcanic rocks also occurred in this region (Jia, 2014; Liu et al., 2015d). Consequently, the contribution from the deep source cannot be ruled out.

In summary, the sulfur in this deposit comes from different reduction mechanisms. In stage I, the sulfur is dominantly produced by bacterial sulfate reduction (BSR) of seawater or sulfate minerals. As for stage II-III, the sulfur is dominantly produced by the thermochemical sulfate reduction (TSR) of seawater or sulfate minerals.

5.3. Possible sources of ore-forming metals

5.3.1. Constraints from Pb isotopes

Sulfides usually have very low U and Th contents (especially galena), so the radiogenic Pb produced by U and Th is insignificant and tiny (Carr et al., 1995; Muchez et al., 2005; Pass et al., 2014; Zhou et al., 2018c). Meanwhile, compared with the traditional mineral analyses of Pb isotopes, the in situ Pb isotope analysis is convenient and free from impurity inclusions, so it can more truthfully reflect the Pb isotopic compositions of ore-forming fluids.

In the $^{206}Pb/^{204}Pb$ vs. $^{207}Pb/^{204}Pb$ diagram (Fig. 11A), the Pb isotopic ratios of sulfides mainly fall into the field between the Pb isotopic evolution lines of orogenic belt and upper crust (Zartman and Doe, 1981). Similarly, in the plot of $^{206}Pb/^{204}Pb$ vs. $^{208}Pb/^{204}Pb$ (Fig. 11B), the Pb isotopic ratios of sulfides mainly fall into the field between the Pb isotopic evolution lines of orogenic belt and lower crust. The above indicates that Pb primarily comes from the orogenic belt and crust (Zartman and Doe, 1981).

Based on previous extensive research on the carbonate-hosted Pb-Zn deposits in the Sanjiang Pb-Zn metallogenic belt, two potential Pb sources have been proposed, that is, the ore-hosting sedimentary rocks and metamorphic basement rocks (Bin et al., 2019; Hao et al., 2015; Jia et al., 2018; Liu et al., 2015a, 2015c, 2015b, 2016, Song et al., 2009, 2013, 2015; Wang et al., 2018b; Xu et al., 2018; Guo, 2018; Hao, 2014; Pan et al., 2003; Qian, 2014; Zhang, 2014). Compared with the sedimentary rocks and basement rocks, all the Pb isotope data fall into the overlapping field of sedimentary rocks and basement rocks (Fig. 11), suggesting a probable mixed Pb source of sedimentary rocks and basement rocks. It means that there is not a single source for the Pb. This explanation is further supported by Sr isotope signatures (see below).

Also, The Pb isotopic compositions of pyrite formed in stage I (Py-I) vary widely (Fig. 11), and their S isotopic compositions suggest that the

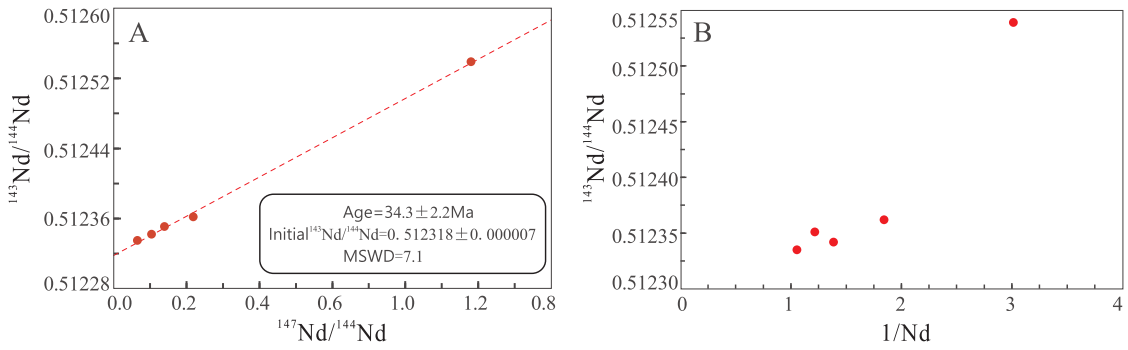

Fig.9. A. Sm-Nd isochron for hydrothermal calcites from the Quemocuo deposit; B. Plot of 1/Nd-$^{143}Nd/^{144}Nd$ for the hydrothermal calcites.

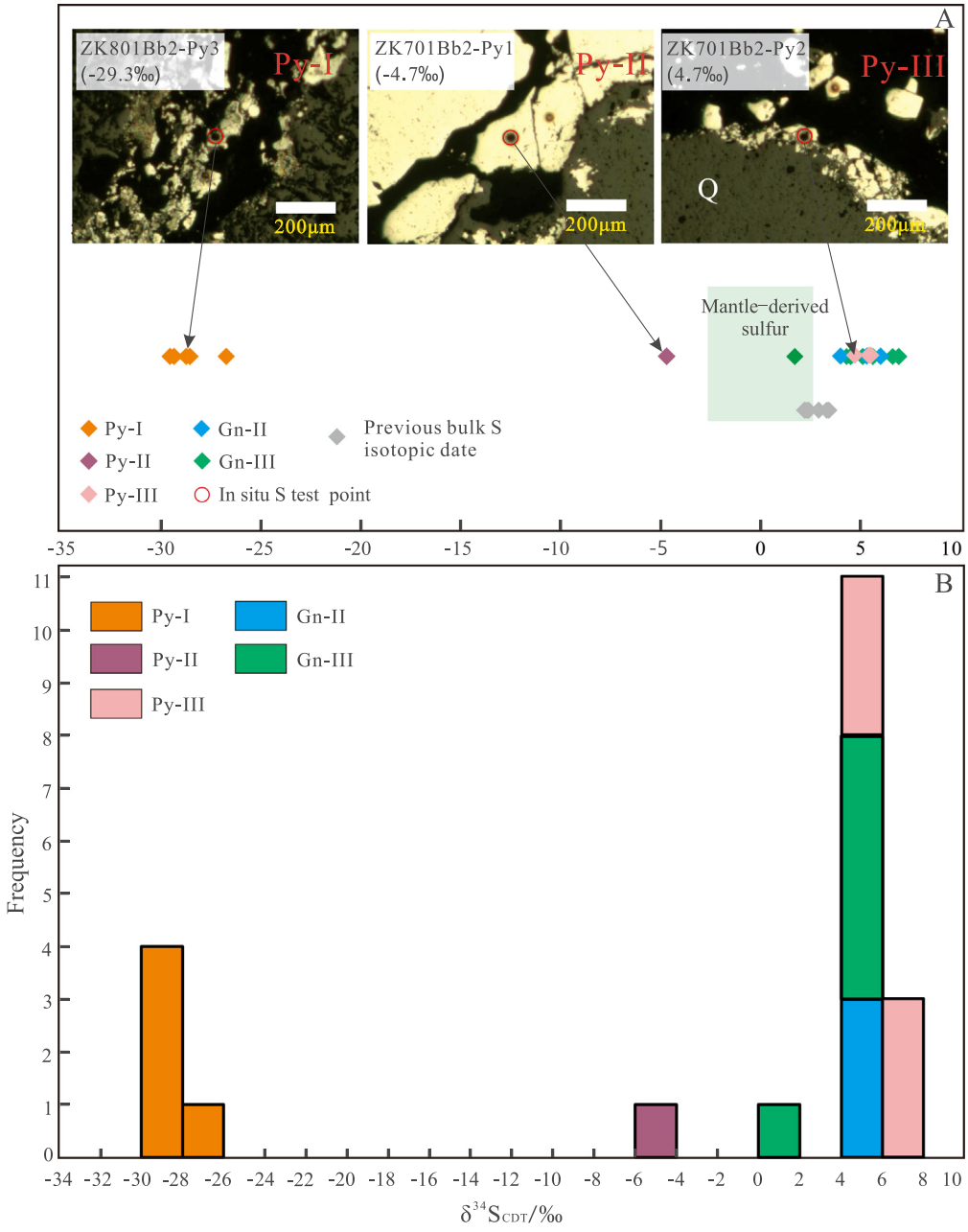

Fig.10. A. The $\delta^{34}S_{CDT}$ values of the Quemocuo deposit that compare with previous data and mantle-derived, showing the in situ $\delta_{34}S$ values for pyrite; B. Sulfur isotopic compositions histogram for the Quemocuo deposit. Previous bulk S isotopic data is from Jia. (2014), mantle-derived S is from Chaussidon et al., (1989).

sulfur source of stage I is mainly from early sedimentary strata. It means that the source of Pb is more complex, except for strata, it may come from a small number of the basement and volcanic rocks, so the variation of isotopic composition for the pyrite in stage I is relatively large (Fig. 11).

Compared with stage I, the Pb isotopic compositions of sulfides formed in stage II-III have a small variation. There is a gradual increase in the $^{206}Pb/^{204}Pb$, $^{207}Pb/^{204}Pb$, and $^{208}Pb/^{204}Pb$ ratios from stage II (Py-II and Gn-II) to stage III (Py- III and Gn- III) (Fig. 12). The Pb isotopic data shows that the variation ranges of $^{206}Pb/^{204}$ Pb, $^{207}Pb/^{204}Pb$, and $^{208}Pb/^{204}Pb$ ratios for the galena (0.179, 0.034 and 0.348; Table 1) and the pyrite (0.142, 0.072 and 0.337; Table 1) in stage II and III are significantly higher than the analytical uncertainty of in situ Pb isotope data for the galena (1 s, 0.001–0.004, 0.001–0.004 and 0.003–0.011, respectively) and the pyrite (1 s, 0.002–0.036, 0.002–0.031 and 0.002–0.077, respectively), and this variation should have geological implications. This variation can be explained by the radiogenic Pb existed in the sulfides in the late phase (stage III) more than in the early phase (stage II). Therefore, a highly radiogenic Pb-enriched source (such as metamorphic basement rocks) is possible to provide more Pb to the hydrothermal fluids in the late phase. Bin et al. (2019) also suggest that the basement rocks contribute to the ore-forming metals in the late phase for the Pb-Zn deposit in Lanping area.

In general, in situ lead isotopic compositions of pyrite and galena indicate the similar lead origin for three stages (stage I, stage II and stage III), i.e., sourced from strata, strata mixed with a little contribution of metamorphic basement, and strata mixed with a considerable amount of contribution of metamorphic basement, respectively.

5.3.2. *Constraints from Sr isotopes*

The Rb-Sr isotopic compositions of sphalerite can not only effectively constrain the mineralization age of the Pb-Zn deposit, but also

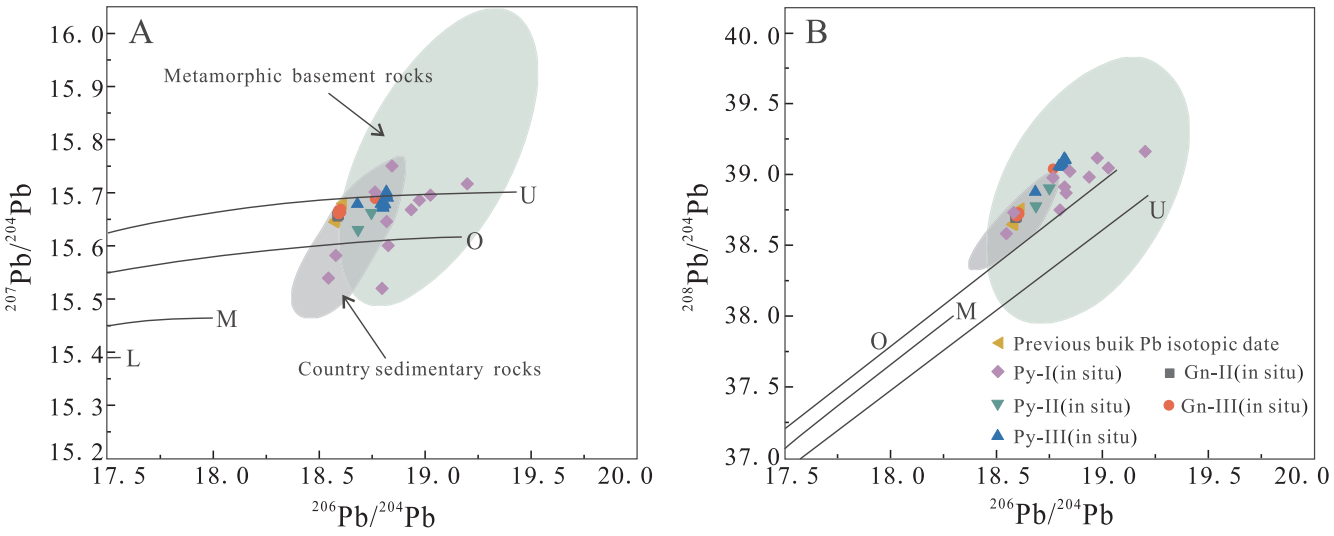

Fig.11. Plots of $^{207}Pb/^{204}Pb$ vs. $^{206}Pb/^{204}Pb$ (A) and $^{208}Pb/^{204}Pb$ vs. $^{206}Pb/^{204}Pb$ (B) that present the field of metamorphic basement rocks, sedimentary rocks (Pan et al., 2003; Tian et al., 2011), and the Pb evolution curves of U, O, M and L (Zartman and Doe, 1981); the Upper Crust (U), Orogen belt (O), Mantle (M) and Lower Crust (L). Bulk Pb isotopic dates are from Jia. (2014).

reflect the source of the ore-forming materials (Brannon et al., 1992; Christensen et al., 1995; Hu et al., 2015; Nakai et al., 1990; Wang et al., 2018a; Wang et al., 2018b; Xiong et al., 2018; Zhou et al., 2015). Although we did not obtain the ideal Rb-Sr isochronic age in this study, the source of the ore-forming fluid can be traced by the Sr isotopic compositions of sphalerite.

According to the contents of Rb and Sr as well as Rb-Sr isotopic compositions of sphalerite, the initial $^{87}Sr/^{86}Sr$ of sphalerite can be

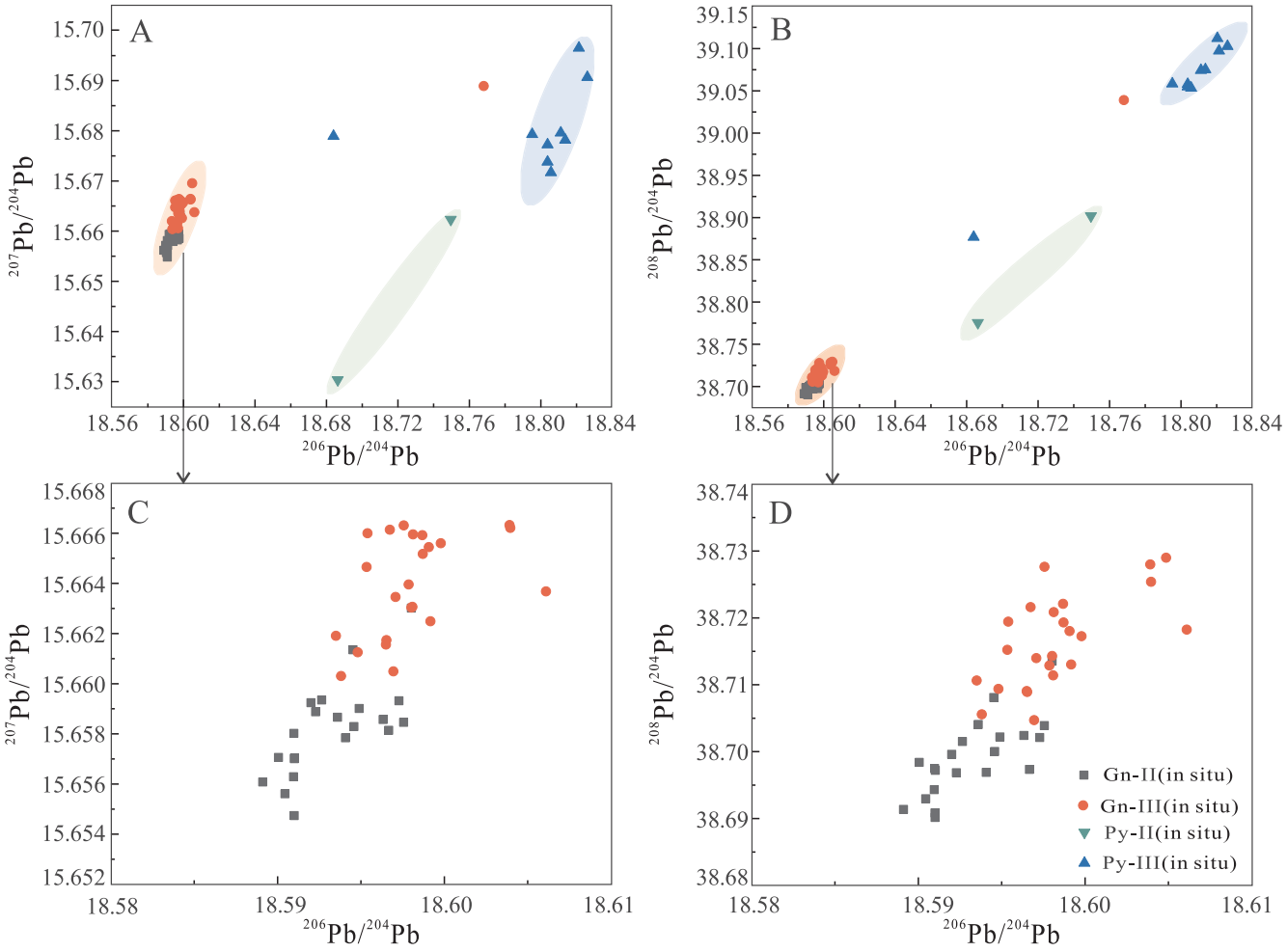

Fig.12. Plots of in situ $^{207}Pb/^{204}Pb$ vs. $^{206}Pb/^{204}Pb$ (A-B) and $^{208}Pb/^{204}Pb$ vs. $^{206}Pb/^{204}Pb$ (C-D) that reveal the variation in Pb isotopes from the early galena-II and pyrite-II to the late galena-III and pyrite-III.

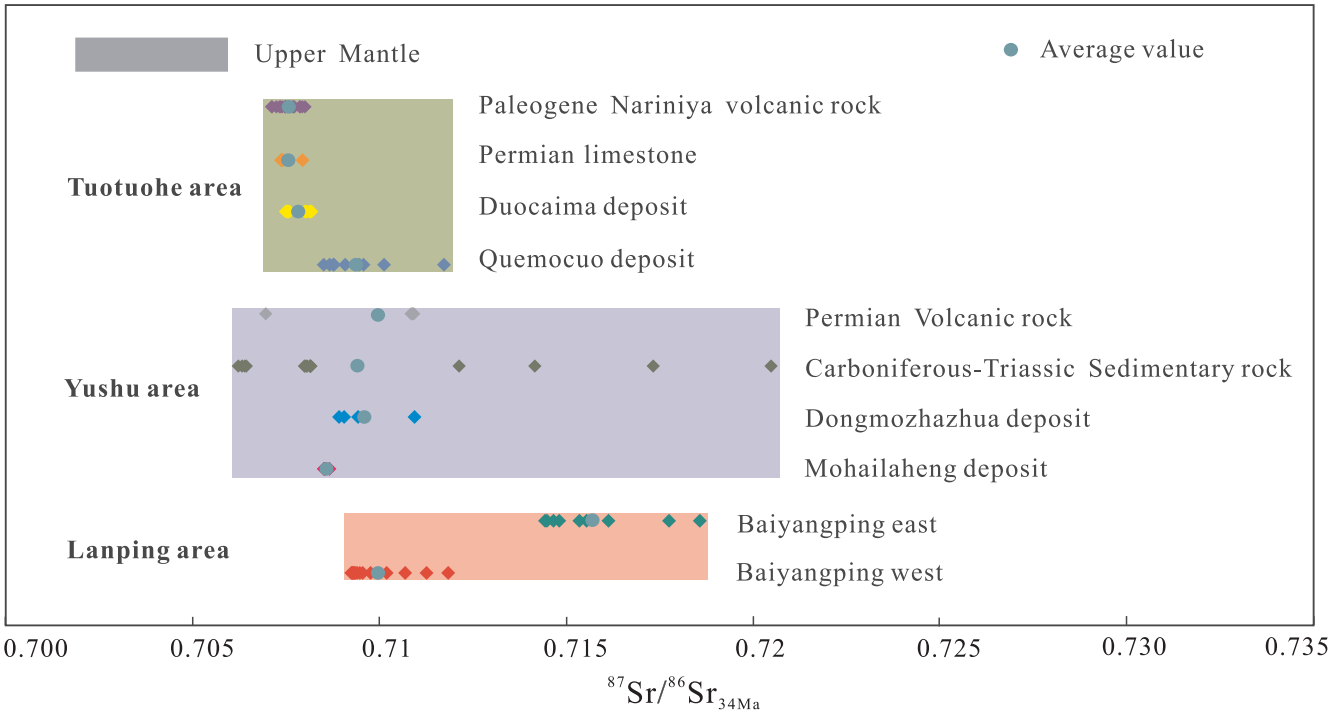

Fig. 13. The $^{87}Sr/^{86}Sr_{34\ Ma}$ ratios of sphalerite and upper mantle, volcanic rock, and sedimentary rock. Data from Feng et al. (2017); Hao et al. (2015); Wang et al. (2011); Zhang (2013); Liu (2012); Qian (2014).

Table 5
Sr isotopes compositions of sulfide, volcanic rock and sedimentary rock.

Mineral/rock	Num.	$^{87}Sr/^{86}Sr_{30Ma}$ range	Average	Source
Sphalerite from the Quemocuo deposit	9	0.7085–0.7117	0.7094	This paper
Calcite from the Duocaima deposit	11	0.7075–0.7082	0.7078	Hao et al.,2015
Permian jiushidaoban Fm., limestone	4	0.7074–0.7079	0.7075	Hao et al.,2015
Sphalerite from the Dongmozhazhua deposit	4	0.7089–0.7109	0.7096	Tian et al.,2014
Sphalerite from the Mohailaheng deposit	4	0.7085–0.7087	0.7086	Tian et al.,2014
Sphalerite and Galena from the Baiyangping east deposit	9	0.7144–0.7186	0.7158	Feng et al., 2017
Sphalerite from the Baiyangping west deposit	14	0.7093–0.7118	0.7099	Wang et al.,2011
Paleogene volcanic rock from the Nariniya	22	0.7071–0.7080	0.7076	Qian, 2014, Zhang, 2013
Permian volcanic rock from the Yushu area	4	0.7069–0.7109	0.7099	Liu, 2012
Carboniferius-Triassic Sedimentary from the Yushu area	17	0.7062–0.7204	0.7095	Liu, 2012

$(^{87}Sr/^{86}Sr)t = {}^{87}Sr/^{86}Sr - {}^{87}Sr/^{87}Rb\ (e^{\lambda t}-1)$, $\lambda_{Rb} = 1.41 \times 10^{-11} t^{-1}$, t = 34 Ma. Fm. = Formation.

calculated by combining the mineralization age of about 34 Ma obtained by calcite Sm-Nd dating. The initial $^{87}Sr/^{86}Sr$ of sphalerite is 0.708482–0.711723 (Table 4), which is higher than the initial Sr isotopic compositions (t = 34 Ma) of the mantle, and the Paleogene volcanic rocks and Permian limestone in the Tuotuohe area (Fig. 13 and Table 5), implying that the single source cannot reasonably explain the Sr isotopic composition of sphalerite. The sulfur and lead isotopic compositions of sulfides suggest that ore-forming materials and fluids are likely to be multi-sourced, including metamorphic basement and strata, and a small number of volcanic rocks (deep source). However, it is somewhat hard to trace the source of ore-forming material based on initial Sr isotopic compositions of sphalerite at present, because of the lack of Rb-Sr isotopic data for metamorphic basement. In the same metallogenic belt, the Baiyangping deposits have the same source as the Quomocuo deposit, containing much higher initial $^{87}Sr/^{86}Sr$ ratios than those of country sedimentary rocks and volcanic rocks (Fig. 13). Therefore, we propose that Sr isotope features support the involvement of the metamorphic basement and strata in mineralization, while the metamorphic basements should have a relatively high initial $^{87}Sr/^{86}Sr$ isotopic composition. Furthermore, based on the similarity of Hg isotopic compositions between the sulfides from sediment-hosted Pb-Zn deposit and metamorphic basement in the Changdu and Lanping area (east of the Quemocuo deposit), Xu et al. (2018) and Bin et al. (2019) suggest that Hg in sulfides was mainly originated from the metamorphic basement. Besides, there are no exposed Permian volcanic rocks in the study area, the Sr isotopic data of Permian volcanic rocks in the Yushu area is similar to that of Quemocuo lead-zinc deposit, we cannot rule out the contribution of volcanic rocks to lead-zinc mineralization.

It is noticed that the initial Sr isotopic compositions of Pb-Zn deposit in the Tuotuohe area are comparable to the Pb-Zn deposit in Yushu and Lanping area, with some differences to some degree. It is likely that the variation in the contribution proportion of the metamorphic basement, strata, and volcanic rocks lead to fluctuation of Sr isotopic compositions in different Pb-Zn deposits in different regions of the Sanjiang Pb-Zn metallogenic belt. Additionally, the Sr isotopic compositions of the metamorphic basement, strata, and volcanic rocks in the Quemocuo area and the Sanjiang Pb-Zn metallogenic belt need to be further studied to better constrain the source of Sr for the Pb-Zn deposit.

In summary, the Sr isotopic compositions of the Quemocuo Pb-Zn deposit may be derived from the country sedimentary rocks depleted in initial $^{87}Sr/^{86}Sr$ relatively as well as the metamorphic basement rocks enriched in initial $^{87}Sr/^{86}Sr$ relatively.

Table 6
A comparison between typical MVT deposits and Quemocuo Pb-Zn deposit.

Characteristics	MVT deposits	Quemocuo Pb-Zn deposit
Grades	Pb + Zn: av. < 10 wt%	Pb + Zn: av. 2.92 wt%
Host rocks	Cambrian to Carboniferous carbonate rocks	Upper Permian carbonate rocks
Tectonic settings	Typically located within extensional zones of orogenic belts	Typically places within the middle zone of the thrust-nappe structure
Relation with magmatic activity	absence of temporally or spatially association with igneous activities	Spatially and temporally association with the Cenozoic magmatic activity
Ore-controlled factors	Mainly controlled by open structure and lithology	Controlled by structure and lithology
Ages	From Proterozoic to Cretaceous	34 Ma
Ore textures and structures	Exhibiting disseminated, fine grained, branched, colloidal and massive structures and colloidal, skeleton coarse-crystalline textures	Mainly exhibiting massive, brecciated, disseminated, veined structures, and grained textures
Mineral compositions	Sphalerite, galena, pyrite, barite, fluorite, dolomite and calcite	Sphalerite, galena, pyrite, calcite, bournonite, dolomite and barite
Fluid inclusions	10–30 wt% NaCl equiv.; 50–200 °C	2.4–17.3 wt% NaCl equiv.; 160–260 °C
Associated metals	Ag	Ag
C–O isotopes	Sourced from carbonate rocks	Sourced from carbonate rocks
S isotopes	+10 to +25‰, sourced from seawater sulfate	−30 to +8‰, sourced from multiple S reservoirs
Pb isotopes	Complicated Pb isotopic ratios and regional zonation, soured from basements and sediments	Complicated and simple Pb isotopic ratios, sourced from basements, strata and volcanic rocks (deep source)
Sr isotopes	Imply that the fluids were derived from, flowed through or interacted with multiple reservoirs	Imply that the fluids were derived from basements, strata and volcanic rocks (deep source)
References	Leach et al., 2005, 2010	Jia, 2014, Liu et al., 2015d, This paper

5.4. Genesis of the deposit and mineralization process

5.4.1. Ore genesis

The Qumocuo Pb-Zn deposit with a low grade (Pb + Zn < 10 wt%) is hosted by Upper Permian strata, and the mineralization is controlled by lithology and structure (Jia, 2014; Liu et al., 2015d; Table 6). Sphalerite + galena + calcite/dolomite + barite as major minerals and ore-forming fluids have a medium salinity (Jia, 2014; Liu et al., 2015d; Table 6), which are comparable to those of the typical MVT Pb-Zn deposits (Leach et al., 2005; 2010). However, compared with the typical MVT deposits, the Qumocuo Pb-Zn deposit is located in the middle of the thrust belt and is closely related to the structural deformation (Jia, 2014; Liu et al., 2015d; Table 6). Moreover, this deposit is associated with the Paleogene potassic magmatic rock temporally and spatially (Jia, 2014; Qian, 2014; Liu et al., 2015d; Table 6). In situ S, Pb and Sr isotopic compositions of sulfides in this study suggest that the metamorphic basement and strata, and even volcanic rocks are the main sources of ore-forming elements. Furthermore, fluid inclusion homogenization temperatures of quartz obtained by Jia (2014) are 160–260 °C with the main range of 160–220 °C. The above features indicate that the Qumocuo Pb-Zn deposit is somewhat different from the typical MVT Pb-Zn deposits (Leach et al., 2005, 2010). Therefore, combined with the regional background, the ore deposit geology, and S-Pb-Sr isotopic compositions, we classify this deposit as an epigenetic, carbonate-hosted and normal fault-controlled Pb-Zn deposit.

5.4.2. Ore-forming process

The formation of the Quemocuo deposit is associated with thrust system, and the mineralization age is similar to other Pb-Zn deposits in the Sanjiang Pb-Zn metallogenic belt, which are different from typical MVT deposits that have no spatial and temporal relationship with igneous activity (Leach et al., 2005, 2010). Based on field investigation, the geology of deposit, calcite Sm-Nd dating, in situ S and Pb isotopic compositions of sulfides, Rb-Sr isotopic compositions of sphalerite, we speculate that the ore-forming process of Quemocuo Pb-Zn deposit as follows:

The Cenozoic India-Eurasian continental collision resulted in the development of thrust system in Qiangtang block (Fig. 14A), accompanied by the formation of a series of Cenozoic sedimentary basins, potassic magma and Pb-Zn mineralizations (Yin and Harrison, 2000; Deng et al., 2001; Zhao et al., 2004; Zhu et al., 2006; Zhao et al.,2007; Yang et al., 2008; Li et al., 2006, 2012; Liu, 2012, Liu et al., 2015e, 2016, 2017; Zhang, 2014; Song et al., 2015; Qian, 2014).

At c.a. 34 Ma, the Pb-Zn mineralization in the Tuotuohe area was also linked to the Cenozoic Tanggula thrust system occurred during 52–23 Ma (Li et al., 2006, Liu, 2012) and potassic magmatic rocks occurred in the period of 40–32 Ma (Qian, 2014), where the Quemocuo Pb-Zn deposit was located at the middle of the Tanggula thrust system in the Tuotuohe area (Fig. 14B). The NW-trend and NE-trend faults formed in the Quemocuo area have played an important role in controlling the distribution of Pb-Zn mineralization (Jia, 2014; Liu et al., 2015d). Thermal activity related to this event resulted in the circulation of hydrothermal fluids within strata and metamorphic basement, where they picked up metals, migrated upward along regional faults to the shallow depth, and precipitated metals. The fluids and ore-forming materials came from different sources and played a very important role in the formation of sulfides at different stages (Figs. 10–13). We have classified three metallogenic stages, i.e., 1) in stage I, the sulfur is from the bacterial sulfate reduction (BSR) of seawater or sulfate minerals and the source of ore-forming elements derived from strata, and even a small number of volcanic rocks and metamorphic basement; 2) in stage II, the sulfur is from the thermochemical sulfate reduction (TSR) of seawater or sulfate minerals and the ore-forming elements sourced from strata mixed with a little contribution of metamorphic basement; 3) in stage III, the source of sulfur and ore-forming elements are similar to those in stage II, but the contribution of metamorphic basement materials were moderately increased.

Moreover, we cannot rule out the contribution from the contemporaneous potassic magmatism. Contemporaneous magmatism may mainly as heat sources or provide ore-forming materials.

6. Conclusions

(1) The Sm-Nd dating of calcite shows that the formation age of the Quemocuo Pb-Zn deposit is about 34 Ma, which is similar to other Pb-Zn deposits in the Sanjiang Pb-Zn metallogenic belt and associated simultaneously thrust system.
(2) In-situ S and Pb isotopes suggest that the ore-forming elements are mainly sourced from the metamorphic basement rocks and ore-hosting sedimentary rocks, and even volcanic rocks.
(3) The Quemocuo Pb-Zn deposit is a carbonate-hosted and normal fault-controlled epigenetic deposit.

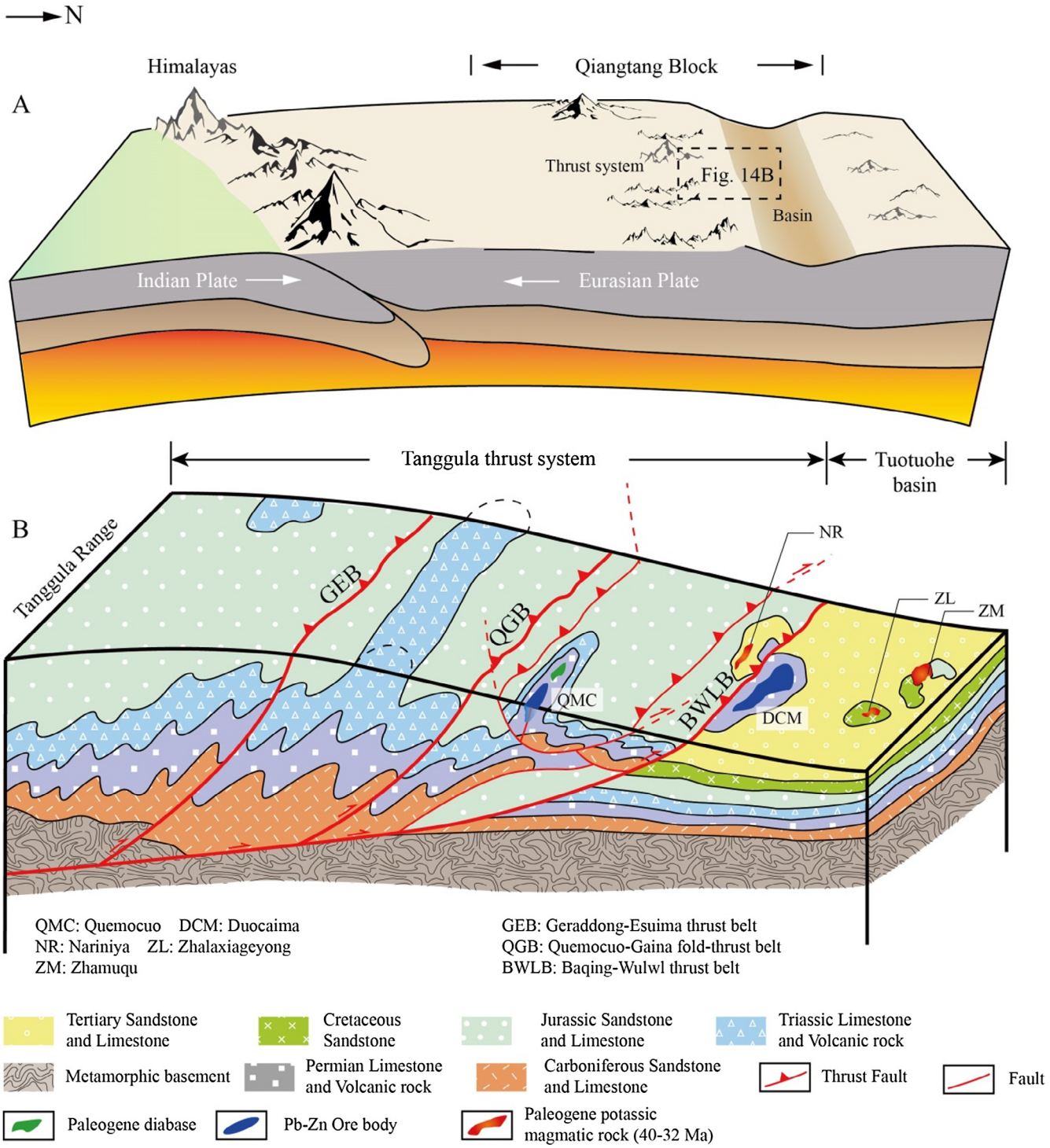

Fig. 14. A metallogenic model of the Quemocuo Pb-Zn deposits in the Tuotuohe area (the Tanggula thrust system model based on the results of Li et al. (2006, 2012) A. The Cenozoic India-Eurasian continental collision resulted in the development of thrust system in Qiangtang block, accompanied by the formation of a series of Cenozoic sedimentary basins, potassic magma, and Pb-Zn mineralizations B. The Cenozoic Tangjula thrust system (occurred during 52–23 Ma) and the Pb-Zn mineralization in the Tuotuohe area formed c.a. 34 Ma.

Acknowledgements

This research was financially supported by the National Key R&D Program of China (2018YFC0604001) and the National Natural Science Foundation of China (41872095, 41802241 and 41430315). We thank Mr. Ming Yan and Mr. Haiming Guo who from the NO.5 Institute of Geology and Mineral Resources Exploration, Xining and work in the Quemocuo mine district. Mr. Shoujian Chen and Mr. Zhongnan Wu who from the Xi'an Center of Geological Survey are thanked for assistance during field work. We are grateful to Dr. Kaiyun Chen, Dr. Zhian Bao, and Dr. Lu Chen who from the Northwest University (Xi'an, China) for helping with LA-MC-ICP-MS S and Pb isotope analysis and Prof. Yinxi Wang from the Nanjing University (Nanjing, China) for helping with Rb-Sr, Sm-Nd isotope analysis. We are grateful for the constructive suggestions and comments from the Editor-in-Chief Prof. Franco Pirajno and anonymous reviewers, which helped us greatly improve the

manuscript.

Appendix A. Supplementary data

Supplementary data to this article can be found online at https://doi.org/10.1016/j.oregeorev.2019.103264.

References

Bao, Z.A., Chen, L., Zong, C.L., Yuan, H.L., Chen, K.Y., Dai, M.N., 2017. Development of pressed sulfide powder tablets for in situ sulfur and lead isotope measurement using LA-MC-ICP-MS. Int. J. Mass Spectrom. 421, 255–262.

Barker, S.L., Hickey, K.A., Cline, J.S., Dipple, G.M., Kilburn, M.R., Vaughan, J.R., Longo, A.A., 2009. Uncloaking invisible gold: use of nanoSIMS to evaluate gold, trace elements, and sulfur isotopes in pyrite from Carlin-type gold deposits. Econ. Geol. 104, 897–904.

Basuki, N.I., Taylor, B.E., Spooner, E.T.C., 2008. Sulfur isotope evidence for thermochemical reduction of dissolved sulfate in Mississippi valley type zinc-lead mineralization, Bongara area, northern Peru. Econ. Geol. 103, 183–799.

Bin, X.W., Tang, Y.Y., Tao, Y., Wang, C.M., Xu, L.L., Qi, H.W., Lan, Q., Mu, L., 2019. Composite metallogenesis of sedimenthosted Pb-Zn-Ag-Cu base metal deposits in the Sanjiang Collisional Orogen, SW China, and its deep driving mechanisms. Acta Petrol. Sin. 35 (5), 1341–1371 (in Chinese with English abstract).

Brannon, J.C., Podosek, F.A., McLimans, R.K., 1992. Alleghenian age of the Upper Mississippi Valley zinc-lead deposit determined by Rb-Sr dating of sphalerite. Nature 356, 509–511.

Carr, G.R., Dean, J.A., Suppel, D.W., Heithersay, P.S., 1995. Precise lead isotope fingerprinting of hydrothermal activity associated with Ordovician to Carboniferous metallogenic events in the Lachlan fold belt of New South Wales. Econ. Geol. 90, 1467–1505.

Chaussidon, M., Albarède, F., Sheppard, S.M.F., 1989. Sulphur isotope variations in the mantle from ion microprobe analyses of micro-sulphide inclusions. Earth Planet. Sci. Lett. 92, 144–156.

Chen, L., Chen, K.Y., Bao, Z.A., Liang, P., Sun, T.T., Yuan, H.L., 2017. Preparation of standards for in situ sulfur isotope measurement in sulfides using femtosecond laser ablation MC-ICP-MS. J. Anal. At. Spectrom. 32, 107–116.

Chen, S.Y., Z, S.Z., Yao, X.D., Jin, X.Y., 2014a. Features of fluid inclusions in Chuduoqu Pb-Zn-Ag Deposit, Qinghai Province and genesis of the deposit. Gold. 10(35), 30-33 (in Chinese with English abstract).

Chen, K.Y., Yuan, H.L., Bao, Z.A., Zong, C.L., Dai, M.N., 2014b. Precise and accurate in situ determination of lead isotope ratios in NIST, USGS, MPI-DING and CGSG glass reference materials using femtosecond laser ablation MC-ICP-MS. Geostand. Geoanal. Res. 38, 5–21.

Chesley, J.T., Halliday, A.N., Kyser, T.K., Spry, P.G., 1994. Direct dating of Mississippi Valley-type mineralization: use of Sm–Nd in fluorite. Econ. Geol. 89 (5), 1192–1199.

Christensen, J.N., Halliday, A.N., Vearncombe, J.R., Kesler, S.E., 1995. Testing models of large-scale crustal fluid flow using direct dating of sulfides Rb-Sr evidence for early dewatering and formation of Mississippi valley-type deposits, Canning Basin, Australia. Econ. Geol. 90, 877–884.

Claypool, G.E., Holser, W.T., Kaplan, I.R., Sakai, H., Zak, I., 1980. The age curves of sulfurand oxygen isotopes in marine sulfate and their mutual interpretation. Chem. Geol. 28, 199–260.

Deng, W.M., Sun, H.J., zhang, Y.Q., 2001. Petrogenesis of Cenzoicpotassic volcanic rocks inNangqen Basin. Chin. J. Geol. 36, 304–318 (in Chinese with English abstract).

Deng, J., Wang, C., Bagas, L., Selvaraja, V., Jeon, H., Wu, B., Yang, L., 2017. Insights into ore genesis of the jinding Zn-Pb deposit, Yunnan Province, China: evidence from Zn and in-situ S isotopes. Ore Geol. Rev. 90, 943–957.

Dill, H.G., Hansen, B.T., Weber, B., 2011. REE contents, REE minerals and Sm/Nd isotopes of granite-and unconformity-related fluorite mineralization at the western edge of the Bohemian Massif: with special reference to the Nabburg-Wölsendorf District, SE Germany. Ore Geol. Rev. 40 (1), 132–148.

Dong, J.L., 2018. Study on Geological Characteristics and Genesis of Basihu Polymetalic Deposit, Tuotuohe area, Qinhai Province. M.S. Dissertation JiLin University (Changchun), Changchun 1-68 (in Chinese with English abstract).

Dong, L.H., Xu, Xi, W., Fan, T.B., Qu, X., Li, H., Wan, J.L., An, H.T., Zhou, G., Li, J.H., Chen, G., Liu, C., 2015. Discovery of the Huoshaoyun super- Large exhalative- sedimentary carbonate Pb- Zn deposit in the Western Kunlun area and its great significance for regional metallogeny. Xinjiang Geol. 33 (1), 41–50 (in Chinese with English abstract).

Feng, C.X., Liu, S., Bi, X.W., Hu, R.Z., Chi, G.X., Chen, J.J., Feng, Q., Guo, X.L., 2017. An investigation of metallogenic chronology of eastern ore block in Baiyangping Pb-Zn-Cu-Ag polylmetallic ore deposit, Lanping Basin, western Yunnan Province. Mineral Deposits 36 (3), 691–704. (in Chinese with English abstract).

Goldhaber, M.B., Kaplan, I.R., 1975. Controls and consequences of sulfate reduction ratesin recent marine sediments. Soil Sci. 119, 42–55.

Guo, H.M., 2018. Geological Characteristics and the Mineralization Enrichment regularity of the DuocaimaPb-Zn Deposit in Naqu, Tibet Autonomous Region. M.S. Dissertation JiLin University (Changchun), Changchun 1-80 (in Chinese with English abstract).

Hao, H.D., Song, Y.C., Li, L.S., Jia, Z.Y., Wang, Y.K., Liu, Q., 2015. Characteristics of Breccias and C-O-Sr-S Isotope Geochemistry of the Duocaima Pb-Zn Deposit in Tuotuohe, Qinghai Province: implications for the Ore-forming Process. Acta Geol. Sin (English Edition) 89, 1568–1587.

Hao, H.D., 2014. Breccia Mineralization and Geochemistry Studies of Duocaima Large Lead-Zinc Deposit in Tuotuohe Area. M.S. Dissertation China University of Geosciences (Beijing), Beijing 1-60 (in Chinese with English abstract).

He, S.P., Li, R.S., Wang, C., Gu, P.Y., Yu, P.S., Shi, C., Cha, X.F., 2013. Research on the formation age of Ningduo Rock Group in Changdu Block: evidence for the existence of basement in the North Qiangtang. Earth Sci. Front. 20 (5), 15–24.

He, L.Q., Song, Y.C., Chen, K.X., Hou, Z.Q., Yu, F.M., Yang, Z.S., Wei, J.Q., Li, Z., Liu, Y.C., 2009. Thrust-controlled, sediment-hosted, Himalayan Zn–Pb–Cu–Ag deposits in the Lanping foreland fold belt, eastern margin of Tibetan Plateau. Ore Geol. Rev. 36, 106–132.

Heijlen, W., Muchez, P., Banks, D.A., Schneider, J., Kucha, H., Keppens, E., 2003. Carbonate-hosted Zn–Pb deposits in Upper Silesia, Poland: origin and evolution of mineralizing fluids and constraints on genetic models. Econ. Geo. 98, 911–932.

Hoefs, J., 2015. In: Stable Isotope Geochemistry, 7th ed. Springer-Verlag, BerlinHeidelberg. DOI:10.1007/978-3-319-19716-6.

Hou, Z.Q., Song, Y.C., Li, Z., Wang, Z.L., Yang, Z.M., Yang, Z.S., Liu, Y.C., Tian, S.H., He, L.Q., Chen, K.X., Wang, F.C., Zhao, C.X., Xue, W.W., Lu, H.F., 2008. Thrust-controlled, sediments-hosted Pb–Zn–Ag–Cu deposits in eastern and northern margins of Tibetan orogenic belt: geological features and tectonic model. Mineral Deposits. 27, 420–441 (in Chinese with English abstract).

Hou, Z., Zhang, H., 2015. Geodynamics and metallogeny of the eastern Tethyan metallogenic domain. Ore Geol. Rev. 70, 346–384.

Hu, Q.Q., Wang, Y.T., Mao, J.W., Wei, R., Liu, S.Y., Ye, D.J., Yuan, Q.H., Dou, P., 2015. Timing of the formation of the Changba-Lijiagou Pb–Zn ore deposit, Gansu Province, China: evidence from Rb–Sr isotopic dating of sulfides. J. Asian Earth Sci. 103, 350–359.

Ikehata, K., Notsu, K., Hirata, T., 2008.In situ determination of Cu isotope ratios in copper-rich materials by NIR femtosecond LA-MC-ICP-MS. J. Anal. Atom. Spectrom. 23, 1003–1008.

Jia, W.B., Li, Y.S., Yan, G.S., Lv, Z.C., Yu, X.F., 2018. Ore genesis of the Duocaima Pb-Zn deposit, Tuotuohe area, Qinghai Province, China: evidences from in situ S and Pb isotopes. Acta Petrol. Sin. 34 (5), 1285–1298.

Jia, Z.Y., 2014. Structural Features and Mineralization of the QueMocuo Pb-Zn Deposit, Qinghai Province. M.Sc Thesis. China University of Geosciences (Beijing), pp.1-66 (in Chinese).

Jiang, S.Y., Slack, J.F., Palmer, M.R., 2000. Sm–Nd dating of the giant Sullivan Pb–Zn–Ag deposit, British Columbiai. Geology 28, 751–754.

Jin, Z.G., Zhou, J.X., Huang, Z.L., Ye, L., Luo, K., Gao, J.G., Chen, X.L., Wang, B., Peng, S., 2016. Ore genesis of the Nayongzhi Pb-Zn deposit, Puding city, Guizhou Province, China: evidences from S and in situ Pb isotopes. Acta Petrol. Sin. 32, 3441–3455 (in Chinese with English abstract).

Leach, D.L., Sangster, D., Kelley, K.D., Large, R.R., Garven, G., Allen, C., Gutzmer, J., Walters, S., 2005. Sediment-hosted lead–zinc deposits: a global perspective. Econ. Geol. 561–607.

Leach, D.L., Bradley, D.C., Huston, D., Pisarevsky, S.A., Taylor, R.D., Gardoll, S.J., 2010. Sediment-hosted lead–zinc deposits in Earth history. Econ. Geol. 105, 593–625.

Li, H., Xu, X.W., Cregor, B., Albert, G.H., Dong, L.H., Fan, T.B., Zhou, G., Liu, L.R., Hong, T., Ke, Q., W, C., Zhang, G.L., Li, H. 2019. Geology and Geochemistry of the giant Huoshaoyun zinc-lead deposit, Karakorum Range, northwestern Tibet. Ore Geol. Rev. 106, 251–272.

Li, W.B., Huang, Z.L., Yin, M.D., 2007. Dating of the giant Huize Zn–Pb ore field of Yunnan province, southwest China: constrains from the Sm–Nd system in hydrothermal calcite. Resource Geol. 57, 90–97.

Li, Y., Wang, C., Yin, H., Yi, H., Shi, H., Lin, J., Zhu, L., Li, X., 2001. Fill models of in theQiangtang composite foreland basin in Qinghai-Xizang plateau, China. Acta Sedimentol. Sin. 19, 20–26 (in Chinese with English abstract).

Li, Y., Wang, C., Yin, H., 2002. Filled sequence and evolution of the Mesozoic Qiangtang composite foreland basin in the Qinghai-Tibet plateau. J. Stratigr. 26, 62–67 (in Chinese with English abstract).

Li, Y.L., Wang, C.S., Yi, H.S., Liu, Z.F., Li, Y., 2006. Cenozoic thrust system and uplifting of the Tanggula Mountain, Northern Tibet. Acta Geol. Sin. 80, 1118–1130 (in Chinese with English abstract).

Li, Y., Wang, C., Zhao, X., Yin, A., Ma, C., 2012. Cenozoic thrust system, basin evolution, anduplift of the Tanggula Range in the Tuotuohe region, central Tibet. Gondwana Res. 22, 482–492.

Li, B., Zhou, J.X., Huang, Z.L., Yan, Z.F., Bao, G.P., Sun, H.R., 2015. Geological, rare earth elemental and isotopic constraints on the origin of the Banbanqiao Zn-Pb deposit, southwest China. J. Asian Earth Sci. 111, 100–112.

Liu, C.Z., Li, S.J., Gao, Y.W., Chen, Y.L., S.J., Guo, H.M., Liu, Q., 2015a. Isotopic Geochemistry and Origin of the Duocaima Lead-Zinc Deposit in the Northtern Sanjiang Area. Acta Scientiarum Naturaliu Universitatis Sunyatseni. 54(1), 136-143 (in Chinese with English abstract).

Liu, C.Z., Guo, H.Y., Sun, F.Y., Qian, Y., Li, B.L., Ma, N., Wu, J.H., Niu, B., 2015b. Geological characteristics and prospecting directions of the Duocaima lead-zinc deposit in Tuotuo river area. China Mining Mag. 24 (12), 74–98 (in Chinese with English abstract).

Liu, D., Zhao, Z., Zhu, D.-C., Niu, Y., DePaolo, D.J., Harrison, T.M., Mo, X., Dong, G., Zhou, S., Sun, C., Zhang, Z., Liu, J., 2014. Postcollisional potassic and ultrapotassic rocks in southern Tibet: mantle and crustal origins in response to India–Asia collision and convergence. Geochim. Cosmochim. Acta 143, 207–231.

Liu, Y.C., Hou, Z.Q., Yang, Z.S., Tian, S.H., Yang, T.N., Song, Y.C., Zhang, H.R., Carranza, E.J.M., 2011. Formation of the Dongmozhazhua Pb-Zn deposit in the thrust-fold setting of the Tibetan plateau, China: evidence from fluid inclusion and stable isotope data. Resour. Geol. 61, 384–406.

Liu, C.Z., Li, S.J., Chen, Y.L., Li, D.P., Gao, Y.W., Guo, H.M., Li, L.S., Wang, Y.K., 2015c. Characteristics and genetic type of fluid inclusion of the duocaima Pb-Zn deposit in Qiangtang Area. Geotectonicaet Metal. 39, 658–1339 (in Chinese with English

abstract).
Liu, C.Z., Jia, Z.Y., Zhang, Q.S., Yan, M., Qian, Y., Zhan, S.Z., 2015d. Geological Characteristics and Genesis of Quemocuo Pb-Zn Deposit in the Northern Segment of Sanjiang Belt, Qinghai Province. Metal Mine. 469, 101–106 (in Chinese with English abstract).
Liu, Y.C., Yang, Z., Tian, S., Song, Y., Zhang, H., 2015e. Fluid origin of fluorite-rich carbonate-hosted Pb–Zn mineralization of the Himalayan-Zagros collisional orogenic system: a case study of the Mohailaheng deposit, Tibetan Plateau. China. Ore Geol. Rev. 70, 546–561.
Liu, Y.C., Hou, Z.Q., Yang, Z.S., Tian, S.H., Song, Y.C., Yu, Y.S., Ma, W., 2016. Geology and chronology of the Zhaofayong carbonate-hosted Pb–Zn ore cluster: Implication for regional Pb–Zn metallogenesis in the Sanjiang belt. Tibet. Gondwana Res. 35, 15–26.
Liu, Y.C., Kendrick, M.A., Hou, Z.Q., Yang, Z.S., Tian, S.H., Song, Y.C., Honda, M., 2017. Hydrothermal Fluid origins of carbonate-hosted Pb-Zn deposits of the Sanjiang Thrust Belt, Tibet: indications from Noble Gases and Halogens. Econ. Geol. 112, 1247–1268.
Liu, Y.C., 2012. Characteristics and Metallogenic Genesis of the Carbonate-Hosted Lead-Zinc Deposits in the Middle Part of Sanjiang Area, Tibetan Plateau. Chinese Academy of Geological Sciences, Beijing, pp. 1–247 (in Chinese with English abstract).
Ludwig, K.R., 2003. User's manual for Isoplot 3.00: a geochronological toolkit for Microsoft Excel.
Luo, K., Zhou, J.X., Huang, Z.L., Wang, X.C., Wilde, S.A., Zhou, W., Tian, L.Y., 2019. New insights into the origin of early Cambrian carbonate-hosted Pb-Zn deposits in South China: a case study of the MalipingPb-Zn deposit. Gondwana Res. 70, 88–103.
Muchez, P., Heijlen, W., Banks, D., Blundell, D., Boni, M., Grandia, F., 2005. Extensional tectonics and the timing and formation of basin-hosted deposits in Europe. Ore Geol. Rev. 27, 241–267.
Nakai, S.I., Halliday, A.N., Kesler, S.E., Jones, H.D., 1990. Rb-Sr dating of sphalerites from Tennessee and the genesis of Mississippi Valley type ore-deposits. Nature 346, 354–357.
Ohmoto, H., 1986. Stable isotope geochemistry of ore deposits. Rev. Mineral. 16, 185–225.
Ohmoto, H., Goldhaber, M.B., 1997. Sulfur and carbon isotopes. In: Barnes, H.L. (Ed.), Geochemistry of Hydrothermal Ore Deposits, third ed. Wiley, New York, pp. 517–611.
Pan G.T., Xu Q., Hou Z.Q, Wang L.Q, Du D.X., Mo X.X., Li D.M., Wang M.J., Li X. Z, Jiang X.S and Hu Y.Z., 2003. Archipelagic orogenesis, metallogenic systems and assessment of the mineral resources along the Nujiang– Lancangjiang–Jinshajiang area in southwestern China. Beijing: Geological Publishing House, 1–420 (in Chinese with English abstract).
Pass, H.E., Cookem, D.R., Davidson, G., Maas, R., Dipple, G., Rees, C., Ferreira, L., Taylor, C., Deyell, C.L., 2014. Isotope geochemistry of the northeast zone, Mount Polleyalkalic Cu-Au-Ag porphyry deposit, British Columbia: a case for carbonate assimilation. Econ. Geol. 109, 859–890.
Peng, J.T., Hu, R.Z., Burnard, P.G., 2003. Samarium-neodymium isotope systematic of hydrothermal calcites from the Xikuangshan antimony deposit (Hunan, China): the potential of calcite as a geochronometer. Chem. Geol. 200 (1), 129–136.
Powell, T.G., Macqueen, R.W., 1984. Precipitation of sulfide ores and organic matter: sulfate reactions at Pine Point. Canada Sci. 224, 63–66.
Qian, Y., 2014. Metallogenic Setting and Metallogenesis of Lead and Zinc in Tuotuohe Region, Qinghai-Tibet Plateau. Ph.D. JiLin University (Changchun), Changchun 1-134 (in Chinese with English abstract).
Seal, I.R., 2006. Sulfur isotope geochemistry of sulfide minerals. Rev. Mineral. Geochem. 61, 633–677.
Song, Y.C., Hou, Z.Q., Li, Z., Yang, T.N., Liu, Y.X., Yang, Z.S., Tian, S.H., Wang, X.H., Wang, G.H., Zhang, H.R., Liu, Y.C., Liu, C.Z., Li, L.Y., Wang, G.R., Wang, Y.K., Zhao, C.X., Liu, Q., 2009. Chaqupacha Pb-Zn ore deposit in Tuotuohe: the product of fluid activity in the basin under continental collision. Acta Mineral. Sin. 29 (S1), 186–187 (in Chinese with English abstract).
Song, Y.C., Hou, Z.Q., Yang, T.N., Li, S.J., Wang, F.C., Gao, Y.W., Gong, X.G., Yang, Z.S., Zhang, H.R., Li, L.S., Wang, G.R., Wang, Y.Q., Liu, Q., Hao, H.D., 2013. Mineral prospecting and its related approaches in Duocaima Pb-Zn deposit, Tuotuohe, Qinghai Province, China. Mineral Deposits 32 (4), 744–756 (in Chinese with English abstract).
Song, Y.C., Yang, T., Zhang, H., Liu, Y., Hao, H., Li, Z., 2015. The Chaqupacha Mississippi Valley-type Pb–Zn deposit, central Tibet: ore formation in a fold and thrust belt of the India-Asia continental collision zone. Ore Geol. Rev. 70, 533–545.
Song, Y.C., Hou, Z.Q., Liu, Y.C., Zhang, H.R., 2017. Mississippi Valley- Type (MVT) Pb-Zn deposits in the Tethyan domain: a review. Geol. China 44 (4), 664–689 (in Chinese with English abstract).
Song, Y.C., Liu, Y., Hou, Z., Fard, Mahmoud, Zhang, H., Zhuang, L., 2019. Sediment-hosted Pb–Zn deposits in the Tethyan domain from China to Iran: Characteristics, tectonic setting, and ore controls. Gondwana Res. 75, 249–328.
Spurlin, M.S., Yin, A., Horton, B.K., Zhou, J., Wang, J., 2005. Structural evolution of theYushu-Nangqian region and its relationship to syncollisional igneous activity, east-central Tibet. Geol. Soc. Am. Bull. 117, 1293–1317.
Su, W.C., Hu, R.Z., Xia, B., Xia, Y., Liu, Y.P., 2009. Calcite Sm–Nd isochron age of the Shuiyindong Carlin-type gold deposit, Guizhou. China. Chem. Geol. 258, 269–274.
Sverjensky, D.A., 1981. The origin of a Mississippi valley-type deposit in the Viburnum Trend, south Missouri. Econ. Geol. 76, 1848–1872.
Tan, S.C., Zhou, J.X., Li, B., Zhao, J.X., 2017. In situ Pb and bulk Sr isotope analysis of the Yinchanggou Pb-Zn deposit in Sichuan Province (SW China): constraints on the origin and evolution of hydrothermal fluids. Ore Geol. Rev. 91, 432–443.
Tang, Y.Y., Bi, X.W., Fayek, M.F., Hu, R.Z., Wu, L.Y., Zou, Z.C., Feng, C.X., Wang, X.S., 2014. Microscale sulfur isotopic compositions of sulfide minerals from the Jinding Zn–Pb deposit, Yunnan Province, Southwest China. Gondwana Res. 26, 594–607.
Tang, J.X., Zhong, K.H., Liu, Z.C., Li, Z.J., Dong, S.Y., Zhang, L., 2006. Intracontinent orogeny and metallogenesis in Himalayan epoch: Changdu large composite basin, Eastern Tibet. Acta Geol. Sin. 80, 1364–1376 (in Chinese with English abstract).
Tian, S.H., Yang, Z.S., Hou, Z.Q., 2011. Sulfur, lead, strontium and neodymium isotope compositions of the Dongmozhazhua lead-zinc ore deposit in the Yushu area, Southern Qinghai: Implications for the sources of ore-forming material in the deposit. Acta Petrol.Sin. 27(7), 2173-2183 (in Chinese with English abstract).
Tian, S.H., Gong, Y.L., Yang, Z.S., Hou, Z.Q., Liu, Y.C., Song, Y.C., Xue, W.W., Lu, H.F., Wang, F.C., Zhang, Y.B., 2014. Rb–Sr and Sm–Nd isochron ages of the Dongmozhazhua and Mohailaheng Pb–Zn ore deposits in the Yushu area, southern Qinghai and their geological implications. Acta Geol. Sin. 88, 558–569.
Uysal, I.T., Zhao, J.X., Golding, S.D., Lawrence, M.G., Glikson, M., Collerson, K.D., 2007. Sm–Nd dating and rare-earth element tracing of calcite: implications for fluid-flow events in the Bowen Basin, Australia. Chem. Geol. 238, 63–71.
Wang, G.R., Song, Y.C., Zhou, G.M., Hou, Z.Q., Yang, Z.S., Yang, T.N., Zhang, H.R., Liu, Y. X., Li, Z., W, Y.K., Liu, Q., RanJian, D.J., Zhao, C.X., Zhai, Z.B., 2012. History, current status, and next targets of exploration in the Chaqupacha Pb-Zn deposit, southern Qinghai Province. Acta Petrologicaet Mineralogica. 31(1), 79-89 (in Chinese with English abstract).
Wang, X.H., Hou, Z.Q., Song, Y.C., Yang, T.N., Zhang, H.R., 2011. Baiyangping Pb–Zn–Cu–Ag polymetallic deposit in Lanping basin: metallogenic chronology and regional mineralization. Acta Petrol. Sin. 27, 2625–2634 (in Chinese with English abstract).
Wang, L.J., Mi, M., Zhou, J.X., Luo, K., 2018a. New constraints on the origin of the Maozu carbonate-hosted epigenetic Zn-Pb deposit in NE Yunnan Province, SW China. Ore Geol. Rev. 101, 578–594.
Wang, X.H., Song, Y.C., Zhang, Liu, H.R., Liu, Y.C., Pan, X.F., Guo, T., 2018b. Metallogeny of the Baiyangping Lead-Zinc Polymetallic Ore Concentration Area, Northern Lanping Basin of Yunnan Province China. . Acta Geol. Sin (English Edition) 92, 1486–1507.
Wang, Y.X., Yang, J.D., Chen, J., Zhang, K.J., Rao, W.B., 2007. The Sr and Nd isotopic variations of the Chinese Loess Plateau during the past 7 Ma: implications for the East Asian winter monsoon and source areas of loess. Palaeogeogr. Palaeoclimatol. Palaeoecol. 249 (3), 351–361.
Wilkinson, J.J., Eyre, S.L., Boyce, A.J., 2005. Ore-forming processes in Irish-type carbonate-hosted Zn-Pb deposits: evidence from mineralogy, chemistry, and isotopic composition of sulfides at the Lisheen mine. Econ. Geol. 100, 63–86.
Woodhead, J., Hergt, J., Meffre, S., Large, R.R., Danyushevsky, L., Gilbert, S., 2009. In situ Pb-isotope analysis of pyrite by laser ablation (multi-collector and quadrupole) ICPMS. Chem. Geol. 262, 344–354.
Worden, R.H., Smalley, P.C., Oxtoby, N.H., 1995. Gas souring by the thermochemical sulfate reduction at 140 °C. AAPG Bull. 79, 854–863.
Xiong, S.F., Gong, Y.J., Jiang, S.Y., Zhang, X.J., Li, Q., Zeng, G.P., 2018. Ore genesis of the Wusihe carbonate-hosted Zn-Pb deposit in the Dadu River Valley district, Yangtze Block, SW China: evidence from ore geology, S-Pb isotopes, and sphalerite Rb-Sr dating. Mineral. Deposita. 53, 967–979.
Xu, C.X., Yin, R.H., Peng, J.T., Hurley, J.P., Lepak, R.F., Gao, J.F., Feng, X.B., Hu, R.Z., Bi, X.W., 2018. Mercury isotope constraints on the source for sediment-hosted lead-zinc deposits in the Changdu area, southwestern China. Mineral. Deposita. 53, 339–352.
Xue, C.J., Zeng, R., Liu, S.W., Chi, G.X., Qing, H.R., Chen, Y.C., Yang, J.D., Wang, D.H., 2007. Geologic, fluid inclusion and isotopic characteristics of the Jinding Zn–Pb deposit, western Yunnan, South China: a review. Ore Geol. Rev. 31, 337–359.
Yang, Z.M., Hou, Z.Q., Yang, Z.S., Wang, S.X., Wang, G.R., Tian, S.H., Wen, D.Y., Wang, Z.L., Liu, Y.C., 2008. Genesis of porphyries and tectonic controls on the Narigongma porphyry Mo (-Cu) deposit, southern Qinghai. Acta Petrol. Sin. 24, 489–502 (in Chinese with English abstract).
Yang, W.L., 2017. Mineralization regularity and ore genesis of Duocaima Pb-Zn deposit in Tuotuohe area. M.S. Dissertation JiLin University, Changchun 1-51 (in Chinese with English abstract).
Yao, X.D., Zhang, S.C., Zhang, Z.L., Si, J.Y., 2019. Metallogenic Model of Duocaima Lead-zinc Deposit in Sanjiang Metallogenic Belt of Southwest China. China's Manganese Ind. 37 (1), 55–58 (in Chinese with English abstract).
Ye, L., Cook, N.J., Ciobanu, C.L., Liu, Y., Zhang, Q., Liu, T., Gao, W., Yang, Y., Danyushevskiy, L., 2011. Trace and minor elements in sphalerite from base metal deposits in South China: a LA-ICPMS study. Ore Geol. Rev. 39, 188–217.
Yin, A., Harrison, T.M., 2000. Geologic evolution of the Himalayan-Tibetan orogen. Annu. Rev. Earth Planet. Sci. 28, 211–280.
Yuan, H.L., Chen, K.Y., Bao, Z.A., Zong, C., Dai, M., Fan, C., Yin, C., 2013. Determination of lead isotope compositions of geological samples using femtosecond laser ablation MC-ICP-MS. Chin. Sci. Bull. 58 (32), 3914–3921.
Yuan, H.L., Yin, C., Liu, X., Chen, K.Y., Bao, Z.A., Zong, C.L., Dai, M.N., Lai, S.C., Wang, R., Jiang, S.Y., 2015. High precision in-situ Pb isotopic analysis of sulfide minerals by femtosecond laser ablation multi-collector inductively coupled plasma mass spectrometry. Sci. China Earth Sci. 58, 1713–1721.
Zartman, R.E., Doe, B.R., 1981. Plumbotectonics-the model. Tectonophysics 75, 135–162.
Zhang, C., 2013. Study on the metallogensis of the Nariniya lead-zinc deposits, Tuotuohe, Qinghai. M.S. Dissertation. East China Institute of Technology, pp. 1–65.
Zhang, C.Q., Wu, Y., Hou, L., Mao, J.W., 2015. Geodynamic setting of mineralization of Mississippi Valley-type deposits in world-class Sichuan–Yunnan–Guizhou Zn–Pb triangle, southwest China: implications from age-dating studies in the past decade and the Sm–Nd age of Jinshachang deposit. J. Asian Earth Sci. 103, 103–114.
Zhang, S.C., Yan, M., Liu, Q., 2008. Geological characteristics and genesis of the Nabaozhalong lead-zinc deposit in Anduo, Tibet. Sci. Technol. Inf. 16, 33–34 (in Chinese with English abstract).
Zhang, H.R., Yang, T.N., Hou, Z.Q., Song, Y.C., Liu, Y.C., Yang, Z.S., Tian, S.H., 2017. Structural controls on carbonate-hosted Pb-Zn mineralization in the dongmozhazhua deposite, central Tibet. Ore Geol. Rev. 90, 863–876.

Zhang, H.R., 2010. Deformational Structures and Metallogenetic Model of Sediment-Hosted Pb-Zn Deposits in Northern Segment of the Sanjiang Orogentic Belt, Southwest China. M.S. Dissertation China Academy of Geological Science (Beijing), Beijing 1-94 (in Chinese with English abstract).

Zhang, H.S., 2014. Study of ore-controlling structures of Pb-Zn deposit in the Tuotuohe area, Qinghai Province. M.S. Dissertation China University of Geosciences (Beijing), Beijing 1–65 (in Chinese with English abstract).

Zhao, Z.D., Mo, X.X., Dong, G.C., Zhou, X., Zhu, D.C., Liao, Z.L., Sun, C.G., 2007. Pb Isotopic Geochemistry of Tibet an Plateau and Its Implications. Geoscience 21 (2), 265–272 (in Chinese with English abstract).

Zhao, X., Yu, X.H., Mo, X.X., Zhang, J., Lu, B.X., 2004. Petrological and geochemical characteristics of Cenozoic alkali-rich porphyries and xenoliths hosted in western Yunnan province. Geoscience 18, 217–228 (in Chinese with English abstract).

Zhou, J.X., Huang, Z.L., Bao, G.P., Gao, J.G., 2013. Sources and thermo-chemical sulfate reduction for reduced sulfur in the hydrothermal fluids, southeastern SYG Pb–Zn Metallogenic Province, SW China. J. Earth Sci. 24, 759–771.

Zhou, J.X., Bai, J.H., Huang, Z.L., Zhu, D., Yan, Z.F., Lv, Z.C., 2015. Geology, isotope geochemistry and geochronology of the Jinshachang carbonate-hosted Pb-Zn deposit, southwest China. J. Asian Earth Sci. 98, 272–284.

Zhou, J.X., Luo, K., Li, B., Huang, Z.L., Yan, Z.F., 2016a. Geological and isotopic constraints on the origin of the Anle carbonate-hosted Zn-Pb deposit in northwestern Yunnan Province, SW China. Ore Geol. Rev. 74, 88–100.

Zhou, J.X., Dou, S., Huang, Z.L., Cui, Y.L., Ye, L., Li, B., Gan, T., Sun, H.R., 2016b. Origin of the LupingPb deposit in the Beiya area, Yunnan Province, SW China: constraints from geology, isotope geochemistry and geochronology. Ore Geol. Rev. 72, 179–190.

Zhou, J.X., Wang, X.C., Wilde, S.A., Luo, K., Huang, Z.-L., Wu, T., Jin, Z.-G., 2018b. New insights into the metallogeny of MVT Pb-Zn deposits: a case study from the Nayongzhi in South China, using field data, fluid compositions, and in situ S-Pb isotopes. Am. Mineral. 103, 91–108.

Zhou, J.X., Xiang, Z.Z., Zhou, M.F., Feng, Y.X., Luo, K., Huang, Z.L., Wu, T., 2018a. The giant Upper Yangtze Pb–Zn province in SW China: Reviews, new advances and a new genetic model. J. Asian Earth Sci. 154, 280–315.

Zhou, J.X., Luo, K., Wang, X.C., Wilde, S.A., Wu, T., Huang, Z.L., Cui, Y.L., Zhao, J.X., 2018c. Ore genesis of the Fule Pb-Zn deposit and its relationship with the Emeishan Large Igneous Province: evidence from mineralogy, bulk C-O-S and in situ S-Pb isotopes. Gondwana Res. 54, 161–179.

Zhou, C.X., Wei, C.S., Guo, J.Y., 2001. The source of metals in the Qilingchang Pb-Zn deposit, Northeastern Yunnan, China: Pb-Sr isotope constraints. Econ. Geol. 96, 583–598.

Zhu, T., 1999. Sedimentary evolution from back-arc to foreland basin: an example from the Qiangtang Mesozoic basin in Northern Xizang, Tethyan. Geology 23, 1–15 (in Chinese with English abstract).

Zhu, G.Y., Fei, A.G., Zhao, J., Liu, C., 2014. Sulfur isotopic fractionation and mechanismfor thermochemical sulfate reduction genetic H2S. Acta Petrol. Sin. 30, 3772–12786.

Zhu, L., Wang, C., Zheng, H., Xiang, F., Yi, H., Liu, D., 2006. Tectonic and sedimentary evolution of basins in the northeast of Qinghai-Tibet Plateau and their implication for the northward growth of the Plateau. Palaeogeogr, Palaeoclimatol, Palaeoecol. 241, 49–60.

Zou, G.M., Li, S.J., Li, L., Qian, Y., Li, L.S., 2014. Characteristics of Fluid Inclusions and Ore Genesis of Chuaduoqu Pb-Zn Ore Deposit in Tuotuohe Ares, Qinghai Province. Northwestern Geol. 47 (4), 256–262 (in Chinese with English abstract).